1-1-2010

A Nondestructive Study Of A Carbon Fibre Epoxy Composite Plate Using Lock-In Thermography, Cyclic Loading, And Finite Element Analysis

Muhammad Saleem
Ryerson University

A NONDESTRUCTIVE STUDY OF A CARBON FIBRE EPOXY COMPOSITE PLATE USING LOCK-IN THERMOGRAPHY, CYCLIC LOADING, AND FINITE ELEMENT ANALYSIS

by

Muhammad Saleem

B.Sc. (Mechanical Engineering)

NWFP University of Engineering & Technology, Peshawar, Pakistan

A Thesis

Presented to Ryerson University

in partial fulfillment of the

requirements for the

Degree of Master of Applied Science

in the Program of

Mechanical Engineering

Toronto, Ontario, Canada, 2010

Author's Declaration

I hereby declare that I am the sole author of this thesis.

I authorize Ryerson University to lend this thesis to other institutions of individuals for the purpose of scholarly research.

I further authorize Ryerson University to reproduce this thesis by photocopying or by other means, in total or in part, at the request of other institutions or individuals for the purpose of scholarly research.

Acknowledgements

I am highly indebted to my colleagues, friends and instructors who provided me all the help I needed to complete this thesis.

First, I wish to express my deep sense of gratitude to my supervisor Dr. Habiba Bougherara for her guidance and support throughout this effort and the honour given to me to work on this project. In addition, Dr. Habiba Bougherara must be credited for sparking my interest in research and also has been a wonderful influence on my career. I am thankful for her much-needed encouragement that helped me see this thesis through.

Dr. Rad Zdero, my co-supervisor, shared his invaluable technical knowledge during the laboratory phase of this study and the use of the laboratory at St. Michael's Hospital, Toronto.

Mr. Suraj Shah provided his precious time and expertise in experimental work of infrared thermography and strain gauges. His cooperation and guidance was necessary to this study which would be not possible otherwise. Mr. Suraj Shah provided me with useful input that enriched my understanding and enthusiasm on the field.

I am grateful to Ms. Leah Rogan and the School of Graduate Studies at Ryerson University, for their assistance throughout the course of my post-graduate studies.

Last, but certainly not least, I recognize my parents and wife for their selfless and absolute support in good times and bad.

Abstract

A NONDESTRUCTIVE STUDY OF A CARBON FIBRE EPOXY COMPOSITE PLATE USING LOCK-IN THERMOGRAPHY, CYCLIC LOADING, AND FINITE ELEMENT ANALYSIS

Muhammad Saleem, B.Sc. Engineering

A thesis presented to Ryerson University in partial fulfillment of the requirements for the degree of Master of Applied Science in the program of Mechanical Engineering

Toronto, Ontario, Canada, 2010

The goal of this study was to validate the results from infrared thermographic experiment by strain gauge experiments and finite element analysis (FEA) in a carbon epoxy composite plate within the linear elastic limit. A FE model of the plate was first developed and subjected to static loads. The strain values were recorded at four distinct points. Then an experiment using strain gauges was carried out for similar loading conditions and the strains were noted for the corresponding locations. The slope of the correlation plot between the FEA and strain gauge static results indicated that, although the strain gauge experimental values had an overall tendency to overestimate the strain, there was a strong correlation between the data as exhibited by the Pearson coefficient R^2 = 0.99. Then the stresses calculated from the strain gauge experiment under cyclic tensile loads were used to validate the results from lock-in thermography. These results also showed good agreement as R^2 was 0.87 and strain gauges experiment tended to underestimate the stress values. From this study, it can be concluded that lock-in thermography can be used to assess stresses in biomaterials used in medical application.

This page is intentionally left blank

Table of Contents

Author's Declaration ii
Acknowledgements iii
Abstract iv
Table of Contents vi
List of Figures x
List of Tables xii
Units Used xiii
Commonly used Terminology xiv
List of Abbreviations xv
Nomenclature xvi
CHAPTER 1. INTRODUCTION 1
1.1 Background 1
1.2 Thesis organization 3
CHAPTER 2. LITERATURE REVIEW 5
2.1 Overview 5
2.2 Nondestructive Inspection Techniques 5
2.2.1 IR Thermography Techniques 6
2.3 Principle of IR Thermography 6
2.4 Basic Temperature Measurement Theory for Infrared Thermography 7
2.4.1 Emissivity 8
2.4.2 Kirchoff's Law 9
2.4.3 Stephan-Boltzmann's Law 9
2.4.4 Planck's Law 10
2.4.5 Heat Transfer 10
2.5 Introduction to Infrared Spectrum 11
2.6 Historical Perspective of Infrared Thermography 12
2.7 Infrared Thermography 13
2.7.1 Passive Thermography 13

2.7.2 Active Thermography 14
2.7.2.1 Classification of Active Thermography 15
2.7.2.2 Lock-in Thermography 15
2.8 Advantages of Lock-in Thermography 16
2.9 Pros and Cons of IR Thermography 17
2.10 Application of Infrared Thermography 17
2.11 Thermal Camera 18
2.12 Classifications of Data Measurement with Infrared Thermal Camera 19
2.13 Composite Materials 20
2.13.1 Introduction 20
2.13.2 Fibre 22
2.13.3 Matrix 23
2.13.4 Carbon Fibre and Epoxy Resin Composite 25
CHAPTER 3. CURRENT STUDY 26
3.1 Motivation 26
3.2 Research Question 27
3.3 Aims and Novelty of this Study 27
CHAPTER 4. STRAIN GAUGES 28
4.1 Experimental Study, Strain Gauges 28
4.2 Strain Gauge Selection 29
4.3 Location of Strain Gauges 30
4.4 Strain Gauge Installation Procedure 30
4.4.1 Degreasing 31
4.4.2 Surface Abrading 31
4.4.3 Gauge layout lines 31
4.4.4 Conditioning 31
4.4.5 Neutralizing 31
4.4.6 Strain Gauge Preparation 31
4.4.7 Strain Gauge Bonding 32
4.4.8 Wiring and Data Acquisition 32
4.5 Sensitivity of Strain Gauge 34

4.6 Strain Gauge Experimental Summary 35
CHAPTER 5. LOCK-IN THERMOGRAPHY EXPERIMENTS 37
5.1 Experimental Setup for the Current Study 37
5.1.1 Description of Thermal Camera Used in the Current Study 39
CHAPTER 6. FINITE ELEMENT ANALYSIS 41
6.1 Background of Finite Element Analysis 41
6.2 Geometric Modelling of Composite Plate 41
6.2.1 Geometry of Carbon Fibre Reinforced Epoxy Composite 41
6.3 Material Properties 42
6.4 Simulation Using ANSYS 42
6.4.1 Boundary Conditions 42
6.5 Mesh Sensitivity and Convergence 43
CHAPTER 7. RESULTS AND DISCUSSION 45
7.1 Experimental and FEA Results 45
7.1.1 Strain Gauge Test Results (Static Loading) 45
7.1.2 Surface Strains values from FEA (Static Loading) 45
7.1.3 Strain Gauge Test Results (Cyclic Loading) 46
7.1.4 Lock-in Thermographic Test Results (Cyclic Loading) 47
7.2 Analysis of Current Study 47
7.2.1 Analysis of Experimental and FEA Strain Measurements (Static Loading) 47
7.2.2 Analysis of LT and Strain Gauge Experimental Measurements (Cyclic Loading) 49
7.2.3 Analysis of Lock-in Thermographic Stress Maps using Cyclic Loading 51
7.3 Discussion 53
7.3.1 Current Study 53
7.3.2 Strain Gauge Experiment versus FEA 53
7.3.3 Strain Gauge versus Lock-in Thermographic Experiments 54
7.4 Comparing the FEA Results with the Literature 54
7.5 Comparing the Strain Gauge Results with the Literature 56
7.6 Limitations and Future Work 56
CHAPTER 8. CONCLUSION 58
APPENDICES 59

APPENDIX 1: Results from Strain Gauge Experiment and Finite Element Study 59
APPENDIX 2: Finite Element Analysis Stress Maps 64
APPENDIX 3: Comparison of Stress values from Strain Gauges and IR Tests 67
REFERENCES 69

List of Figures

Figure 2-1 Diffusion and detectability [47]. 7
Figure 2-2 Wavelengths of the infrared spectrum [58] 11
Figure 2-3 The electromagnetic spectrum [61] 12
Figure 2-4 The circular region indicates the presence of metallic foil in laminated composites [31] 14
Figure 2-5 Experimental arrangements for lock-in thermography 15
Figure 2-6 Phase shift in flaws detection with lock-in thermography 16
Figure 2-7 Application of IR thermography to FRP composite, (A) Thermal image of FRP surface showing defects and (B) cross-section view showing air voids [54] 20
Figure 2-8 Comparison of typical damage zones at notches in metals and composite [111] 21
Figure 2-9 Continuous and discontinuous fibres [114] 22
Figure 2-10 Schematic representation of thermoset polymer 24
Figure 4-1 Strain gauge Locations on Composite Plate 28
Figure 4-2 Geometry and dimensions of specimens with circular holes 28
Figure 4-3 Vishay® 350-Ohms strain gauge model CEA-06-125UW-350 [127] 29
Figure 4-4 Two-Channel DSub-15-Pin Connector attached to Wiring from Two Strain Gauges 32
Figure 4-5 Three-wire quarter-bridge circuit [131] 33
Figure 4-6 Soldering illustration of three Lead Wire Conductors to a Strain Gauge [132] 33
Figure 4-7 DSub-15s Connected to the CRONOS-PL Unit 33
Figure 4-8 UNI2-8, all-purpose eight-channel amplifier 34
Figure 4-9 Cyclic loading application on carbon epoxy rectangular plate 35
Figure 4-10 Instron® FastTrack™ 8874 36
Figure 4-11 Instron® FastTrack™ 8800 Controller Panel 36
Figure 5-1 Infrared experimental setup 38
Figure 5-2 Lock-in Thermography process [24] 39
Figure 6-1 Carbon epoxy composite rectangular plate 41
Figure 6-2 Boundary conditions on the assembly, Force direction is indicated by the red arrow. 43
Figure 6-3 From top to bottom, mesh relevance, 100, 80, 60, 40 and 20% for the Composite plate 43

Figure 7-1 Correlation of all Strain values (excluding location 1) from FEA and Experimental results 49
Figure 7-2 Correlation graph of stress values for all IR and experimental data 51
Figure 7-3 Stresses along line 1 and 2 are shown in the graph for average 1000N cyclic tensile load..... 52
Figure 7-4 Stresses along line 1 and 2 are shown in the graph for average 1500N cyclic tensile load..... 52
Figure 7-5 Stress distribution of woven fabric composite subject to a tensile load for specimen [±45°] [143] 55
Figure 7-6 Stress distribution (FEA) for carbon epoxy composite plate for 1000N tensile load..55
Figure A1- 1 Graphic representation of experimentally measured microstrain values for tensile static loading for strain gauges 60
Figure A1- 2 Graphic representation of calculated microstrain values for tensile static condition in FEA..... 61
Figure A1- 3 Graph of measured microstrain values for 1000N and 1500N for cyclic loading .. 61
Figure A1- 4 Graph of Stress (MPa) values calculated from strain gauge experiment for 1000 N and 1500 N cyclic loading 62
Figure A1- 5 Applied load–displacement curve for 1000N (average) load..... 62
Figure A1- 6 Applied load–displacement curve for 1500 N (average) load..... 63
Figure A2- 1 Normal stress (MPa) in the composite plate for 1000 N..... 64
Figure A2- 2 Normal stress (MPa) in the composite plate for 2000 N..... 65
Figure A2- 3 Normal stress (MPa) in the composite plate for 3000 N..... 66
Figure A3- 1 Graph for LT results for 1000N and 1500N cyclic loading 68

List of Tables

Table 2-1 Thermal conductivities for different materials [45] 8
Table 2-2 Emissivity of some common materials [36] 9
Table 2-3 Matrix materials commonly used in composites [117] 23
Table 4-1 Vishay® 350-Ohms strain gauge specifications [128] 30
Table 5-1 Technical date of Silver 420 Camera [137] 40
Table 6-1 Elastic properties of Carbon fibres/epoxy resin [6, 122, 139-142] 42
Table 6-2 Number of Nodes and elements of different meshes for various relevance 44
Table 7-1 Experimentally measured microstrain values in tensile static loading 45
Table 7-2 Microstrain values calculated from FEA 46
Table 7-3 Measured microstrain values for tensile cyclic loading 46
Table 7-4 Stress values calculated from strain gauge experiment 47
Table 7-5 Stress values from LT experiment for 1000 N and 1500 N cyclic loading 47
Table 7-6 Comparison of FEA and experimental Strain values for static loading 48
Table 7-7 Comparison of stress values obtained from lock-in thermography and Strain gauge .. 50
Table A1- 1 Strain results from the FEA and Strain gauge experimental study for 1000 N 59
Table A1- 2 Strain results from the FEA and Strain gauge experimental study for 2000 N 59
Table A1- 3 Strain results from the FEA and Strain gauge experimental study for 3000 N 60
Table A1- 4 Strain values for all FEA and strain gauge experimental results 63
Table A3- 1 IR and calculated stress values from strain gauge readings for cyclic tensile load of 1000N 67
Table A3- 2 IR stress values and calculated stress values from strain gauge reading for cyclic tensile load of 1500N 67
Table A3- 3 Stress values for all LT and strain gauge experimental results 68

Units Used

^{0}C	Degree centigrade
ohms	A unit of electrical resistance
µm	Micrometer, a unit of length equal to one thousandth (10^{-3}) of a millimeter or one millionth (10^{-6}) of a meter
MPa	Mega Pascal
GPa	Giga Pascal
g/m^3	Surface density
W/mK	Thermal conductivity
kg	Kilogram
J-s	Joule-seconds
kW	Kilowatt
kN	Kilonewton
Hz	Hertz (One cycle per second)
$\mu\varepsilon$	Microstrain ($\varepsilon \times 10^{-6}$)(mm/mm)

Commonly used Terminology

Radiometer	Any instrument for the detection or measurement of radiant energy
Modulation	It is the process of varying one or more properties of a high frequency periodic waveform, called the carrier signal, with respect to a modulating signal
Microbolometer	It is a device used as a detector in a thermal camera. Unlike other types of infrared detecting equipment, microbolometers do not require cooling
Miniature Stirling Engine	MSI (Taiwan) recently developed it as a cooling system especially for personal computer chips that uses the waste heat from the chip to drive a fan
Indium antimonide	It is a crystalline compound made from the elements indium (In) and antimony
Grey scale	In photography grey scale digital image is an image in which the value of each pixel is a single sample, that is, it carries only intensity information
Layup	Arrangement of fibre layers in various plies of composite material [1-2].

List of Abbreviations

NDT	Nondestructive testing
LT	Lock-in Thermography
LCD	Liquid-crystal display
CRT	Cathode-ray tube
IR	Infrared
Hz	Hertz
CF	Carbon fibre
FE	Finite element
FEM	Finite element method
CT	An X-ray technique for producing cross-sectional image of the body Computer tomography or computed axial tomography;
AC	Alternating current
DC	Direct current
IRT	Infrared Thermography
PPT	Pulse Phase infrared Thermography
SGTF	Stress generated thermal field
EATF	Externally applied thermal field
FRP	Fibre reinforced polymer
GFRP	Graphite fibre reinforced polymer
PT	Pulse infrared thermography
TRIR	Time-resolved infrared radiometry
ULT	**U**ltrasound lock-in thermography
PMC	Polymeric matrix composites
GF	Gauge factor
NIR	Near Infrared
BNC	Bayonet Neill-Concelman

Nomenclature

E	Elastic modulus / Modulus of elasticity / Young's modulus
N	Number of loading cycles
V_f	Fibre volume fraction
t	Ply thickness
G	Shear modulus
R_G	Gauge resistance
ΔR	Change in gauge resistance
L	Length
W	Width
T	Thickness
h	Planck's constant
V	Volt, the symbol used for potential difference
k	Stefan-Boltzmann constant
c	Speed of light
K	Kelvin
λ	Wavelength
Δ	Change in a property; usually followed by the notation of the property
ε	Strain
v	Poisson's ratio
v_{xy}, v_{yz}, v_{xz}	Poisson's ratio of multi-layer composite laminates in the global x-, y-, and z-direction
ρ	Resistivity of a conductor
$\mu\varepsilon$	Microstrain ($\varepsilon \times 10^{-6}$)

CHAPTER 1. INTRODUCTION

1.1 Background

Composite materials are widely used in high-performance applications such as, aerospace, automotive and other engineering constructions [3]. Aircraft engine rotor blades were the first components manufactured from composite materials in 1960 [4]. A composite material brings several functional advantages that makes it more particular than other materials, such as its well-documented fatigue and corrosion durability [5], higher mechanical and thermal properties, good strength-to-weight ratio, high stiffness to weight ratio, electrical and heat insulation and long life cycle [4, 6-8]. The mechanical and thermal properties of the composite materials are being modified and enhanced by continuous improvement and research.

The life and stability of a material or a structure is governed by constant or variable loading patterns [9]. Structural reliability of composite components is achieved when the effect of stress concentration is completely understood around design features such as holes and cut outs. The holes and the cut outs are commonly found in structural applications, which create stress and strain concentration areas resulting in weakening of mechanical properties [10].

In order to evaluate mechanical properties, various destructive and nondestructive testing (NDT) are performed on these structural applications. NDT ensures that the structure is free of flaws and defects detrimental to its safety, without damaging the structure. NDT greatly relies on probability of detection of high-strength materials and their defects [11]. NDT, in present aerospace and automotive applications, where the use of carbon fibre reinforced composite is increasing frequently, becomes difficult when flaws are not visible from the outside surface; however, they still could be the reason for failure. For inspection of such damages, the conventional NDT methods like x-ray or ultrasound cannot constantly satisfy all the requirements of inspection. Thus, fast and effective techniques for inspection in industrial environments and in other engineering and bio-mechanics fields are required. Presently, the NDT evaluation techniques consist of infrared thermography, ultrasonic, shearography [11-15] and strain gauges [16], which comply with those requirements. Each technique has its own particular areas of application and advantages, in Chapter 2 thermography is discussed in detail.

In large series of NDT techniques, infrared thermography is broadly used for composite materials [7]. Infrared thermography is a non-contact, non-intrusive, non-destructive evaluation technique, that-aims at revealing subsurface anomalies [17-20], due to temperature difference on the concerned surface and recording these anomalies during scanning by an infrared camera [21]. The fundamental concept of IR thermography is that all components emit electromagnetic radiation at the temperature above absolute zero. These electromagnetic radiations are used to achieve the knowledge of various properties pertaining to the surface [22]. The damaged area heats up quicker than the rest of the body because of the broken thermal path, and its thermal properties are generally different from those of the bulk material. Specific heat, thermal conductivity, thermal diffusivity, and thermal effusivity are important thermal properties [21].

The damage is revealed in shape of the temperature maps, which are generated after detailed analysis of the temperature field with the help of thermographic images. Conduction, convection and radiation help in the rejection of heat generated by the material but the temperature of plastic deformed region remains at an elevated temperature compared to the rest of the body. Infrared camera enables the prediction of the damaged location beforehand due to temperature distribution in the specimen and also helps in monitoring the extent of the damage as it develops [23]. Due to sophistication and advancement in thermographic system, there is an increase in its usage in nondestructive evaluation technique [13] for the measurement of depth defects [24].

Thermographic methods are mainly classified on the basis of the thermal object activation. Basically there are two approaches used for thermography, active and passive [14, 22]. Active thermography can be further divided into various types, such as lock-in thermography, pulse thermography, pulse phase thermography, and vibrothermography.

Passive thermography is broadly used to measure operating temperatures of structures or equipment during preventative maintenance applications, whereas active thermography is normally chosen for NDT or quality assurance applications [25]. Passive thermography is used to detect temperature variation on surfaces without any damage to the component [26]. Active thermography needs an exterior stimulated thermal supply used to record the body temperature for investigation of subsurface defects or voids [27]. Energy can be obtained from a laser, a heater, a hot air blower, a high power thermal pulse, mechanical or electromagnetic sources.

The objective of this study is to investigate the stress distribution in an orthotropic carbon fibre epoxy composite with a circular hole. The geometry was subjected to finite element analysis. The results obtained from infrared thermography were compared with the results obtained from strain gauge results

1.2 Thesis organization

This thesis is organized into 8 main chapters and 3 appendices.

- In Chapter 1, the importance of Infrared Thermography in NDT is discussed. A brief introduction of this thesis is also stated in Chapter 1.

- Chapter 2 provides a description of NDT techniques. Fundamental concepts of infrared thermography are reviewed. This chapter also discusses the concept of heat transfer used in the thermographic process. Further, the infrared spectrum, historical perspective, principles, applications of infrared thermography is discussed. Active and passive thermographic techniques are also described here. The lock-in thermography as an active technique is explained in detail, followed by classifications of data measurement with infrared thermal camera. The theory behind the thermal camera is also discussed. Basic concepts of composite material with special focus on carbon/epoxy composite material is also given.

- Chapter 3 lays out the motivation for the research and aim of this study.

- Chapter 4 describes the experimental study of the strain gauges, preparation of the test surface and mounting of the strain gauge on a composite plate.

- Chapter 5 describes the lock-in thermography test procedure, and description of the thermal camera.

- Chapter 6 displays the CAD modeling of the required composite plate geometry and describes the simulation done with the help of finite element analysis.

- Chapter 7 provides the results of experimental and finite element studies, and discusses their validation, limitations of this study, and a brief commentary on possible future work based on this study.
- Chapter 8 concludes with the summary of the entire study.
- Appendices and references cited in this study are detailed at the end.

CHAPTER 2. LITERATURE REVIEW

2.1 Overview

Different nondestructive (NDT) techniques are being used for a variety of materials. In this chapter, the most common NDT technique of infrared thermography for composite material examination will be reviewed.

The basic theory for temperature measurement by infrared thermography is discussed here. Further, the history and the principle of infrared thermography are also highlighted. Some applications and constraints in thermographic function are also provided. At the end of this chapter, basic concepts of composite material are specified.

2.2 Nondestructive Inspection Techniques

NDT techniques are essential in carrying out analysis of internal properties of the structures without damaging the material and without compromising the service life of the material. It has also received great attention, both for quality control during production and for in-service inspection during maintenance operations.

NDT is used to find damage and flaws such as cracks [28], voids, inclusions [29-30], debonds, improper cure, and delamination [31-32]. NDT techniques such as ultrasonic, visual inspection using borescope [31], thermography, shearography, x-ray [33], C-scan and radiography [28] are employed to assess the defects and to produce a quality component with structural integrity.

The experience of the operator, the type of defect, the material inspected, the inspection condition and the location plays an important role towards the sensitivity and effectiveness of these techniques [34]. NDT techniques are versatile in taking multiple measurements of a moving, fragile, small, hazardous or remote target [35].

Thermography is preferred method because the problems encountered in other NDT techniques such as the reliability of visual inspection [36-37], hazardous effect of x-rays [38], rapid sound attenuation in ultrasound inspection [39], are avoided.

For the current study Infrared (IR) thermographic technique was considered.

2.2.1 IR Thermography Techniques

Measurement of IR radiation distribution on or beneath the surface of a body and converting these measurements into a temperature scale is called thermography. A themogram is a thermal map of a surface captured by a thermal camera by recording IR distribution on the surface. This IR distribution is generated either by stress-generated thermal fields (SGTF) or externally-applied thermal fields (EATF) [40-41].

Thermography is a measurement tool [13, 42], which is based on the principle that the thermal conductivity of a material changes because of flaws and defects present in it.

The infrared thermographic technique is relatively new but it has already gained popularity in various industrial applications such as aerospace, medical diagnostics, electronics, rubber, automotive and construction [40]. It is also used in scientific research programs of geology, archeology, paleontology, bio-speleological discovery, and anthropology [43].

For the current study, the thermographic NDT technique is used for analysis of stress generated by cyclic loading in carbon/epoxy composite plate.

2.3 Principle of IR Thermography

The principle of IR thermography involves heating up the surface of the specimen under investigation. Voids, pores or any type of flaw in the material decreases the thermal conductivities and density [44]. For this purpose, heat is supplied to the specimen, as heat flow rate is one of the functions of properties of the material [45-46], and emitted radiation is recorded by a thermal camera.

If there is any flaw in the material, the isotherms will be curved and non-uniform temperature will be observed near the flaw due to perturbation in the heat flux and temperature field. If the material is defect free then the gradient will be uniform and the isotherm will be a straight line. The location and size of a flaw can be easily detected from the thermogram [45]. This pattern is shown in Figure 2-1.

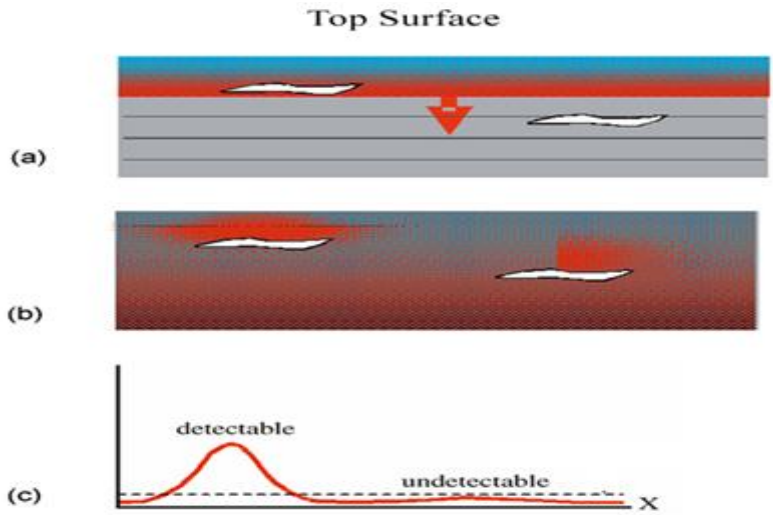

Figure 2-1 Diffusion and detectability: (a) heat generated at the surface propagates into a structure; (b) heat is obstructed by internal anomalies; (c) as the aspect ratio (diameter/depth) of the anomaly decreases, the effect of the anomaly on the surface temperature becomes increasingly difficult to detect, becoming undetectable for temperature differences lower than the noise generated by the camera and background [47].

During IR inspection environmental factors in addition to emissivity coefficient are involved, therefore those factors are also accounted and considered. After considering the environmental factors, the calibration of the system by simulating real operating conditions can be derived as [48],

$$W = \frac{\varepsilon \times A}{e^{B/T} - C} \quad \text{..... Equation 1}$$

where W is detected energy flux, ε is the emissivity coefficient, T is the surface temperature of the object, and A, B and C are the calibration constants which take account of false quantities of energy from or to the environment.

2.4 Basic Temperature Measurement Theory for Infrared Thermography

The theory of IR thermography is that the temperature distribution across the material changes, when the heat flows through the defective portion. This heat flows by means of conduction. Conduction is the main mode of heat transfer within the material as well as from one material to another which is described by Fourier's law, expressed as [45],

$$Q = \frac{k.\Delta T}{t.A_h} \text{ ..... Equation 2}$$

where k is the thermal conductivity of materials, A_h is the specimen's surface area on which the energy is incident, Δ T is change in temperature, and t is the thickness. Heat conduction depends

upon k, higher the k value, higher will be the rate of conduction. FRP composite materials, air gap, or vacuum has lower thermal conductivity as compared to metals [45]. Experiment has proved that for carbon fibre composites, the k value in the plane of the laminate is about 9 times higher than through-thickness direction [49]. A comparison of the thermal conductivities of various materials is given in Table 2-1[45].

Material	Thermal Conductivity (W/mK)
Aluminium	175 – 250
Mild Steel	40 – 75
Concrete	0.8 – 1.2
Brick	0.5 – 1.6
Typical Polymers used in FRP	0.25 – 0.4
Standard/intermediate modulus PAN carbon fibres	20
High modulus PAN carbon fibres	50 – 80
GFRP (V_f = 60%)	0.25 – 0.32
CFRP (V_f = 60%)	0.8 – 1.4
AFRP (V_f = 60%)	0.12 – 0.17

Table 2-1 Thermal conductivities for different materials [45]

IRT depends on emissivity (ε) and surface temperature. IR temperature measurement formulas are mainly based on established and well-proven laws given by Kirchhoff, Stefan-Boltzmann and Planck [44]. Before explaining these theories, emissivity will be discussed.

2.4.1 Emissivity

The emissivity ε is a value to specify how well a real body radiates energy in comparison with a black body at the same temperature and is defined as a ratio of radiation intensities emitted from a real body (sample) and from a black body [50]. It is also known as the ability and efficiency of a material to absorb, reflect or emit energy. The emitting ability depends on factors such as body temperature [51], the particular wavelength [22] being considered for the emitted energy and angle at which the energy is being emitted [44].

Emissivity of the material governs the intensity of the thermal field produced around it [41]. The emissivity of materials ranges from zero to one [22]. For a perfect reflector like a mirrored surface the emissivity is considered to be $\varepsilon = 0$ [36], a black body has $\varepsilon = 1$ and for a real object

(gray body) ε < 1 and greater than zero [44]. Emissivities for some of the common engineering materials are given in Table 2-2.

Material	Emissivity
Steel, Buffed	0.16
Oxidized	0.80
Concrete	0.92
Graphite	0.98
Wood	0.95
Window Glass	0.94

Table 2-2 Emissivity of some common materials [36]

In order to conduct IRT tests, the value of emissivity must be chosen appropriately and according to the material of the specimen. However a sophisticated IR camera itself selects typical values for various engineering materials [52].

2.4.2 Kirchoff's Law

The Kirchoff's law states that the quantity of heat absorbed is equal to the quantity of heat emitted when the body is at the thermal equilibrium [43, 53]. Chemical composition and physical structure of any non-black body establishes the variation from ideal black body behaviour by following Kirchoff's law. It means that if a body does not absorb the entire energy incident upon it, it will radiate less energy than an ideal black body [44].

2.4.3 Stephan-Boltzmann's Law

Stephan-Boltzmann's law describes the relationship between the temperature and the amount of radiation emitted. The law states that the total energy radiated by a black body is directly proportional to the fourth power of the temperature of the body [44]. This means that more IR energy emits when the body is at higher temperature [43].

For a black body, Stephan-Boltzmann's law is expressed as [20],

$$M = \sigma \mathrm{T}^4 \ \frac{J}{m^2 s} \text{ ……..} \qquad \text{Equation 3}$$

where σ is the Stephan–Boltzmann constant and approximately its value is 5.6703 x 10^{-8} W/ (m^2K^4).

The above equation is based upon an ideal black body, when real objects known as grey bodies are considered the above equation will be re written as follows [54]:

$$M = \varepsilon \sigma T^4 \quad \ldots\ldots\ldots\ldots \quad \text{Equation 4}$$

where M is total radiant power emitted by object, ε is emissivity of object's surface and T is the temperature of the object.

2.4.4 Planck's Law

A spectral radiance is defined by Planck's law, and it is the energy emitted by a surface at a given temperature.

An IR camera with proper calibration records this spectral radiance and translates it into temperature distribution using Planck's law [55]. In 1900 Max Planck formulated an equation considering a black body as a perfect emitter as [43, 54],

$$I(\lambda, T) = \frac{2hc}{\lambda^5 \left[\exp\left(\frac{hc}{\lambda KT} \right) - 1 \right]} \quad \ldots\ldots\ldots \text{Equation 5}$$

Where I is spectral radiance, λ is wavelength of emitted radiation, T is absolute temperature of a black body, h is Planck's constant, c is velocity of light in vacuum, and K is Stefan-Boltzmann constant.

2.4.5 Heat Transfer

Transfer of heat from one place to another takes place by three different mechanisms, namely conduction, convection and radiation. Usually heat transfer occurs by a combination of all three modes. For successful thermographic measurements, the phenomenon of each mode of heat transfer must be understood.

Conduction of heat mainly occurs in solids. During this mode of heat transfer, thermal energy is transferred from one place to another by collision of neighbouring molecules.

Convection of heat mainly occurs in fluids, i.e. liquids and gases. In this mode of heat transfer the physical movement of the molecules transfer heat from one place to another.

Radiation of heat occurs in air or vacuum. In this mode, heat energy is emitted from a source in the form of rays or waves. Radiation occurs in the infrared region of the electromagnetic spectrum which can be easily measure by IRT [56].

2.5 Introduction to Infrared Spectrum

Thermal energy or radiation is emitted in the form of electromagnetic waves by all materials in the surrounding environment when their temperature is above absolute zero [52, 57]. Some of the radiation with larger wavelengths and lower energies than the visible spectrum falls in IR spectrum with wavelengths in the range of 0.75 μm to 1000 μm [35]. As these waves are electromagnetic in nature, they do not need medium and they travel with the velocity of light [43]. Rate of radiation is inversely proportional to wave length as shown in Figure 2-2 and it is dependent upon temperature [58].

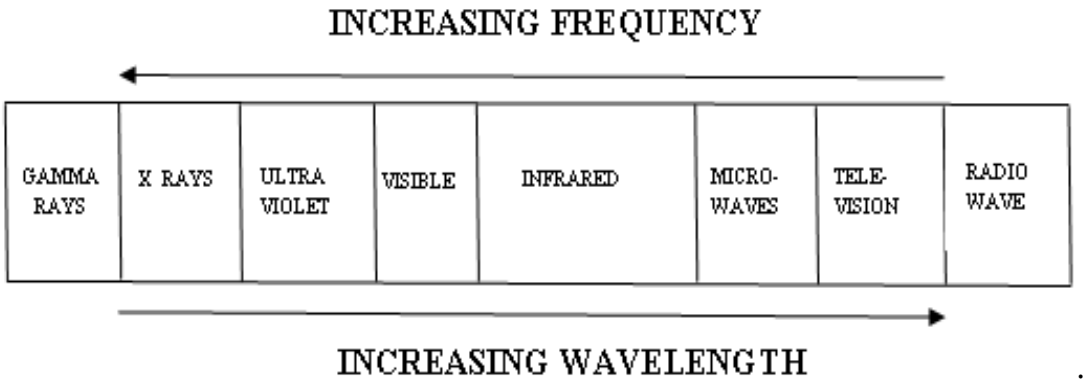

Figure 2-2 Wavelengths of the infrared spectrum [58]

The electromagnetic spectrum encompasses infrared radiation, visible light and ultraviolet light with different wavelengths and frequencies [59]. This electromagnetic spectrum is utilized by thermography between approximately 1 and 14 microns [57]. The IR region is further subdivided as near (0.75– 3 μm), medium (3–6 μm), far (6–15 μm) and extreme infrared (15–100 μm) as shown in Figure 2-3. Far IR is long wave IR which is also called the thermal IR region [60].

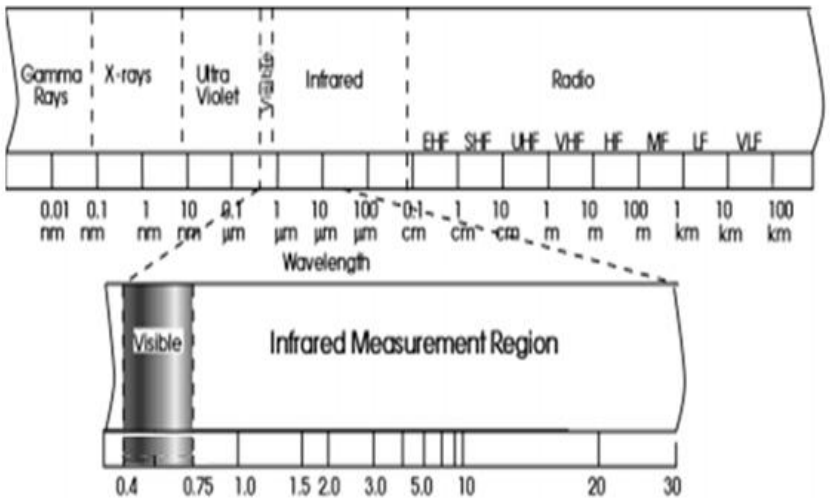

Figure 2-3 The electromagnetic spectrum [61]

The infrared camera was developed in mid-20th century for military application [53, 62]. These cameras can detect radiant energy and can be categorized as short wave infrared (SWIR), middle wave IR (MWIR), and long wave IR (LWIR) [20].

2.6 Historical Perspective of Infrared Thermography

Thermography is thought to be a new NDT method, but in actuality it has a long history that led to the development of the infrared camera. Sir Isaac Newton (1642-1727) was the first person to discover the presence of IR waves [36].

Sir Frederick William Herschel discovered infrared in the 1800s. Herschel dispersed sunlight through a prism into a rainbow spectrum and observed the temperature of each colour from violet to red. He observed that below red light was the hottest region which was not visible to the naked eye. Sir Frederick William Herschel called this invisible radiation calorific ray, known as IR today [43, 63].

In 1860, the black body concept was introduced by German Gustav Kirchhoff. The theoretical existence of electromagnetic waves was predicted by Scot James Clerk Maxwell in 1865. He compared it with light waves.

The relation between the amounts of energy emitted by a black body to the fourth power of its absolute temperature was experimentally found by Slovak Joseph Stefan in 1879, which was theoretically proved by Austrian Ludwig Boltzmann in 1884, and hence named the Stefan–Boltzmann law [20].

In 1967 the field of clinical medical thermography was pioneered and established at Royal Victoria Hospital in Montreal by Dr. R. Lawson [64].

In 1959 the IR camera was first developed by Astheimer and Wormser, using a scanning mirror, a sensitive thermistor, a heat detector, and a rotating chopper. With the help of this camera energy vibrations were developed on a photographic film as a series of varying gray densities [58].

In 1960/61 Gershon-Cohen of Albert Einstein Medical Center started cooperative studies of thermography as a potential diagnostic tool [58].

2.7 Infrared Thermography

IRT is the method by which the temperature of the surface is measured. IR thermography may be successfully employed from the beginning of a manufacturing process [20, 65-69], till the completion of the manufacturing process when the final product is obtained [29, 35, 70] and during the end user maintenance [69, 71-73].

There are many thermographic techniques in use today, which differ from each other on the basis of data acquisition and/or processing. The arrangement of thermographic equipment governs the techniques [74]. EATF thermography (as described in Section 2.2.1) can be further divided into active and passive mode [45]. Details of these techniques are given below.

2.7.1 Passive Thermography

When the temperature of a test material and structure is different from the ambient temperature without external heat source then passive thermography is used. A thermal camera monitors the heat flow, and any variation in the surface temperature indicates the defects in the specimen [47]. The heat flows from the surface is dependent upon the thermal conductivity, location of the defects and variation in the density.

For example if a composite material is tested for defects by thermography, the defective area will transmit less heat and it will be shown as a hot spot in a thermogram. A thermal image of defected laminated surface of carbon/epoxy composite is shown in Figure 2-4 [31].

Passive thermography is widely used for qualitative assessment to detect irregularities and malfunction of the objective [26], and is seldom used for the quantitative measurements of the defect as well [44].

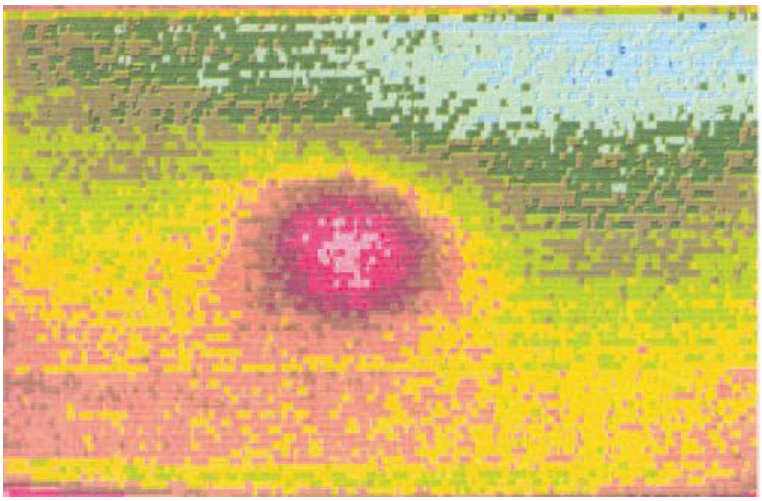

Figure 2-4 The circular region indicates the presence of metallic foil in laminated composites [31]

2.7.2 Active Thermography

Active thermography is a technique in which an external stimulus is applied in order to induce relevant thermal contrasts [47]. It is usually employed when the ambient temperature is not significantly different than the specimen [75]. This external stimulus can be thermal, optical or mechanical [47].

When a body under investigation is externally stimulated by applying heat energy, the heat flows through all layers of that body. If there is any anomaly within different layers of the body, then the rate of flow of heat emitted from it varies. This variation will result in hot and cold spots on the surface of the body [76] which will then be detected using IR thermal camera [36, 46-47].

In optical excitation, the energy from light source such as flash and halogen lamps is delivered to the surface of the specimen where light is transformed into heat [77].

Similarly mechanical oscillation produces heat energy due to friction, which is introduced into the specimen. It is produced either by sonic or ultrasonic transducer [77]. This heat then acts as a thermal stimulus.

2.7.2.1 Classification of Active Thermography

Active thermography is subdivided into Pulse thermography, Pulse phase thermography, Vibrothermography, Step Heating, and Lock-in Thermography [45, 55, 68, 77-78]. For inspection of composite materials usually lock-in thermography is used [55], which is discussed below.

2.7.2.2 Lock-in Thermography

Carlomagno and Berard first introduced the NDT method called lock-in thermography [20, 48, 79]. Later, many researchers further investigated and modified this procedure [15, 19-20, 80-90] of quantitative measurement [65]. Lock-in thermography (LT) was developed to overcome the difficulty of non-uniform heating and variation of the emissivity coefficient of pulse thermography [18].

The LT infrared camera captures the surface temperature of the thermal waves travelling into the material, and a thermal image is created which displays variation of thermal waves [91]. It is suitable for determining material properties and measuring coating thickness [90]. The testing station of LT is illustrated in Figure 2-5 which shows experimental configuration between the camera and the sample.

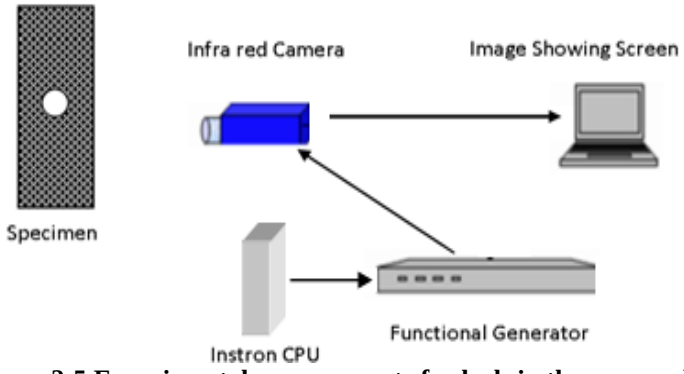

Figure 2-5 Experimental arrangements for lock-in thermography

In lock-in thermography, a thermal wave is produced by periodic energy input and directed towards the test specimen. The surface of the specimen absorbs the wave and shifts the phase as it penetrates deeper. When the wave contacts the defective area, like delamination or inclusions, a portion of it is reflected. The reflected waves interfere with the thermal wave at the surface and create interference patterns [92]. A thermal camera is used to detect the surface radiation, and by evaluating the amplitude and the phase of the local surface temperature a two-dimensional

themogram showing the radiation temperature of the specimen surface, is created, which indicates the internal structure of the specimen [90].

Lock-in thermography is not suitable for thick materials. Thermal waves having lower frequency can penetrate deeper than those having high frequency; this means its sensitivity is dependent upon the frequency [72].

The external excitation sources for heat deposition in LT can be continuous harmonically modulated heating source for example halogen lamps, mechanical vibration [68] or pulse, i.e. flash lamps [88]. In lock-in thermography the temperature data are monitored at a phase shift of each pixel instead of at each pixel itself as shown in Figure 2-6 [54].

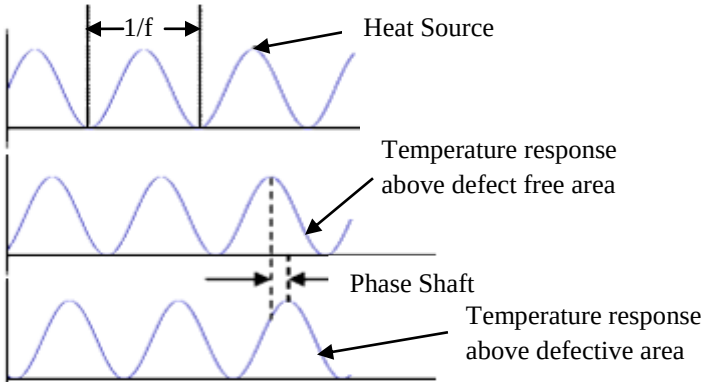

Figure 2-6 Phase shift in flaws detection with lock-in thermography

2.8 Advantages of Lock-in Thermography

Periodic heating gives some advantages in lock-in thermography. Due to concentrated energy at a single frequency this process uses low power thermal waves. LT is a preferred method for NDT application due to amplitude and phase delay properties [86]. Thermal diffusion length gives adjustable depth range in LT. Thermal diffusion length depends upon thermal conductivity, specific heat capacity, lock-in frequency and other material parameters. As lock-in frequency is inversely proportional to the depth of penetration therefore depth can be adjusted by changing the frequency [88]. LT is advantageous in getting information about material composition and indentifies common type of damages like delaminations and impact damage [20]. Long heating and observation time adds to the list of disadvantages of LT [27, 86]. It can also execute investigations by coupling a small quantity of modulated energy into the specimen [92].

2.9 Pros and Cons of IR Thermography

The advantages of thermography are given as follows:

- This method is not hazardous as no harmful radiation emits from this process [93].
- It can be used in a hazardous environment [57].
- It is a non-contact method of thermography [17, 26, 45, 94].
- It is the best and fastest way for investigation of a large area [39, 90].
- It gives instantaneous information [57].
- It is an area investigating technique, unlike other point-to-point and line testing NDT methods [26, 95].
- It is a highly portable method where data can be collected and stored in different digital formats [57, 96-97].
- It is a quantitative analysis method in which captured thermal images contains pixel-by-pixel temperature data [44, 98].

On the other hand, there are some disadvantages of IR thermography, which are given below:

- This method is considered to be difficult to use, hence is not completely exploited [20].
- Thermal losses due to convection and radiation affect the reliability of interpretation of results [94, 98].
- Cost of the equipment is quite high [20, 57, 94, 99].
- Depth of penetration is limited (only a few mm) [22, 44].
- Very high or very low thermal diffusivity and other thermal properties of the materials limit the use of IRT [20].
- The dust particles on the specimen may change the emissivity under inspection which can give spurious results [96].
- Infrared heater needs high power supply [99].

2.10 Application of Infrared Thermography

IR thermography was first used to detect the movement of enemy at night by the military [97]. With the advancement of the technology, IR thermography was used for NDT in the field of engineering [100]. IRT can be used in any area if there is a temperature difference such as in

various industrial productions, maintenance, forest fire detection, medicine, transport industry and land mine detection [76].

It is also used in medical diagnosis to detect metabolic functions of human breast tumors [20, 101] and the temperature change of organs and tissues [97], and as the preliminary diagnostic aid for cancer [40]. IRT is also used to detect any thermal leakages of building envelopes, other building related features [101], and smokestacks for the presence of thermal leaks [102].

In the automobile industry, thermography has been applied to check the performance of IC engines and to investigate air flow through visualization. It is also used to inspect die casting, injection molding, welding and different industrial processes [40]. British-born astronaut Piers Sellers on July 12, 2006, became the first person to conduct thermal NDT in space [103].

2.11 Thermal Camera

In the late 1970s the infrared camera was first used in thermographic NDT [47]. Since then, during the 1980s, continuous improvement has been done on the thermal camera to make it more compatible with black-and-white television signals [90].

The IR camera can capture a temperature variation of less than 0.05 mK [41]. It captures the energy radiated from the surface of the specimen, then calculates and displays this radiation in terms of temperature. The emissivity of the material plays an important role in the measurement of radiation. IR radiations are emitted not only from the specimen itself but also from the surroundings and objects. To minimize its affect on the result of the specimen, different radiation must be taken into account. By providing specimen thermal properties like emissivity of the object, the reflected temperature, the distance between the object and the camera and the relative humidity, the camera can automatically adjust itself and give accurate results [104].

A cooled indium antimonide detector is used in modern infrared cameras having a frame rate of 60 Hz, a focal plane array pixel format of 320 x 256 pixels and an optical lens of 13 mm focal length [22]. The older model cameras have lower frame rates of approximately 1 Hz, low spatial resolution of about 64 x 64 pixels and poor temperature sensitivity of approximately -16 °C [41, 47]**.** Older models of IR cameras use large cooling systems or liquid nitrogen, while, today, systems are using microbolometer technology, miniature stirling engines or remain uncooled

[47]. Thermal cameras are further divided into two kinds based upon detector type. One kind of camera does not require cooling and operates in ambient temperature, while the other kind has cooled detectors containing a cooling unit [105].

Invisible energy radiated from the object is focused on the IR sensitive detector using a lens system build in the thermal camera. The detector measures different energy levels and transforms them into a visible image in different colours or grey scale. LCD or CRT displays these images for viewing by the operator. These images can also be stored for review, analysis and reporting purpose [57].

There are three kinds of detectors in thermal camera, namely, point, linear and array detectors. Array detectors are used more frequently in modern cameras after 1993 [105] and are also called focal plane arrays (FPAs). Commercially available IR cameras produce very high resolution images as they use 75000 detectors for each image [57], which provide hundreds of frames per second and high noise equivalent temperature variation (up to 0.025 °C) [29].

2.12 Classifications of Data Measurement with Infrared Thermal Camera

In the beginning, IR thermography was used for qualitative defect detection only. Now this method is used for quantitative defect detection by improved image processing technique and advanced computing power. It is able to spot the defect location, its severity, along with its impact on the overall structure.

The thermal cameras used for producing qualitative thermograms are also called thermal viewers, while those producing qualitative and quantitative thermograms are called thermal imaging radiometers [56].

In qualitative inspection, thermal images are collected and examined for any sign of non uniformity in the material [56]. Qualitative analysis of a composite material is given as a thermal image in Figure 2-7 [54]. Quantitative inspection is the primary type of IRT data analysis technique. Its principle is to access the defect characteristics by using time dependent temperature data [54].

A thermomechanical force is applied to the specimen and the radiation emitted from the surface of the specimen is then captured and correlated with the stress on the surface [41].

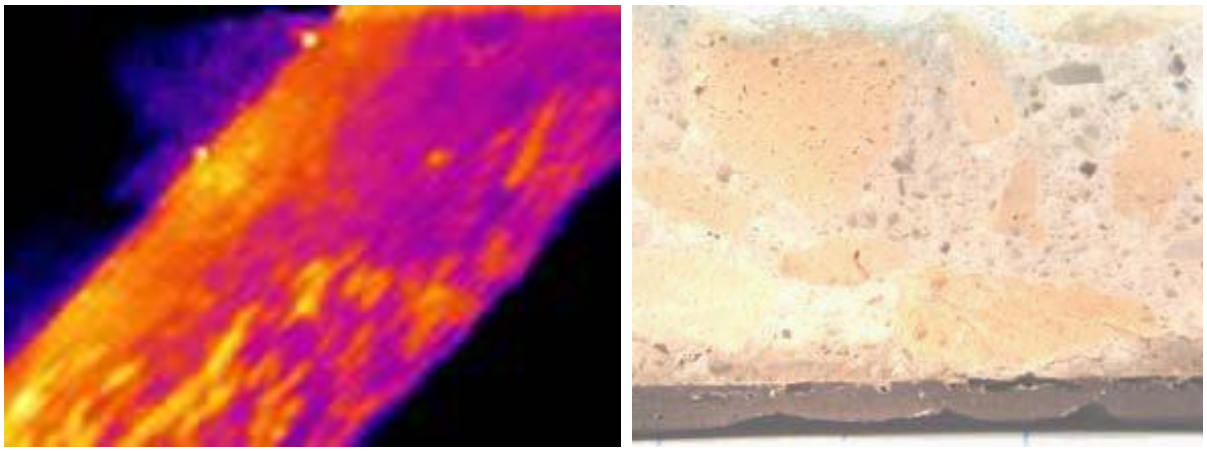

A B

Figure 2-7 Application of IR thermography to FRP composite, (A) Thermal image of FRP surface showing defects and (B) cross-section view showing air voids [54]

2.13 Composite Materials

2.13.1 Introduction

A composite material is formed when two or more elements are combined together to create unique mechanical, thermal and physical properties [106]. They have good engineering properties such as high specific strength, stiffness and lower density. They are widely used in aerospace, marine and automobile industries [107]. Examples of naturally occurring composite materials are wood [106] and bone [108], while steel reinforced concrete and glass reinforced polyester are developed as man-made composite materials. Tailoring of superior mechanical properties and ignoring undesirable qualities is possible in composite materials [106]. High strength and high modulus fibres of composite materials are responsible for carrying maximum load while the resin is the load transfer medium between the fibres [109].

During the 1960s and 1970s much work has been done on the development of continuous fibre composites. Below is a list of some of the advantages of composite materials [110]:

- Higher stiffness and strength of material.
- Better resistance to fatigue damage.
- Easily moldable to acquire any shape prior to cure.

The property of a composite material is dependent upon the nature of carbon fibre and epoxy resin. The carbon fibre provides strength and stiffness whereas epoxy is responsible for chemical and thermal resistance. The load is transferred from epoxy resin to carbon fibre through the

interface when a composite is subjected to stress. For this reason, good interfacial bonding is important, as it governs mechanical properties [107].

The deterioration of the composite material happens in three stages, when subjected to cyclic load. It starts by quick development of damage which contains minute cracks, fibre matrix debonding, fibre pullout from the matrix and other forms of damage. The second stage degradation of the material starts gradually, which is indication of gradual reduction of stiffness. Once the first two stages complete, the material enters into the third stage, where the material experiences fibre breakage and unstable delamination which results in an accelerated decline and finally disastrous failure [111].

From above it is observed that the failure of the composite material is gradual and observable during the damage process, while for metals it is abrupt and sudden which may lead to safety hazards. The difference of failure behaviour of metal and composite material is given in Figure 2-8.

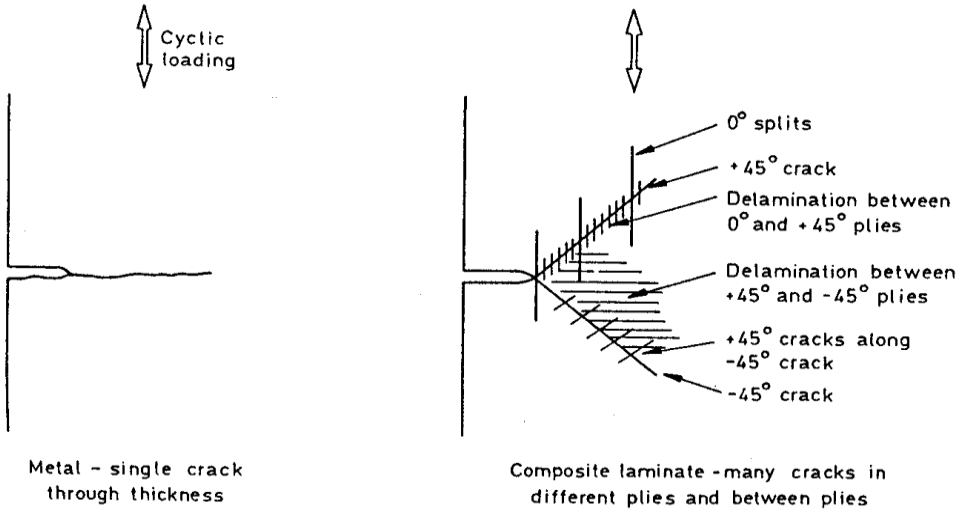

Figure 2-8 Comparison of typical damage zones at notches in metals and composite [111]

Composite materials can be manufactured by autoclave molding, compression molding, resin transfer molding, and filament winding, which are prone to flaws. The defects induced during the manufacturing of the composite materials can be in the fibre (e.g. fibre misalignment, irregular fibre distribution in the cross-section and broken fibres), in the matrix (e.g. voids), and in the interfacial regions (e.g., disbonds and delaminations) [112].

2.13.2 Fibre

In fibre-reinforced composite materials, the fibre is the main component which occupies the largest volume fraction and is responsible for maximum load bearing. Fibre can be either metallic, such as aluminum, copper, iron, nickel, steel or non-metallic like glass, carbon, boron, and graphite.

In the 1950s advanced fibres having high-specific-stiffness (stiffness divided by density) and high-specific-strength (strength divided by density) were developed for structural applications. Aramid, carbon, silicon carbide, alumina are examples of advanced fibres [113].

As shown in Figure 2-9 in linear form the fibres can be either continuous or discontinuous. Continuous fibres are used where the application of fibres is precisely controlled such as filament-wound, pultruded, or laminated structures. Discontinuous or chopped fibres are either mixed directly or combined with a binder to form a planar mat. The fibre orientation is haphazard in discontinuous fibres [113].

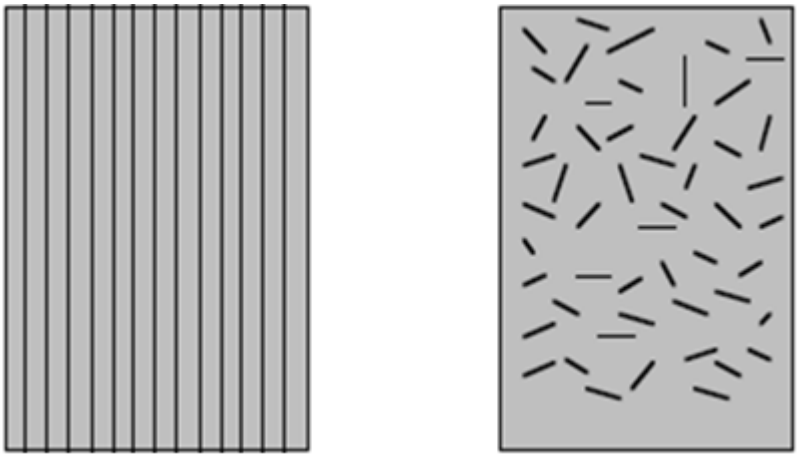

Figure 2-9 Continuous and discontinuous fibres [114]

Strength modulus of carbon fibre is four times higher than the steel while at the same time its density is four times lower. Carbon fibres are anisotropic, brittle, sensitive to damage, waterproof [115] and good electrical conductors [116], hence they are suitable for humid environments. High temperatures up to 1500^{o}C do not comprise its strength [115] while in inert conditions the fibre can be used up to 2500°C [116].

2.13.3 Matrix

The purpose of the matrix in composite material is to keep the fibres bonded, to transfer stress, to provide a barrier against the effect of chemicals and moisture and to protect the surface of the fibres from mechanical degradation [32].

The matrix can be ceramic, metallic or polymeric in nature, as shown in Table 2-3, with different kinds of mechanical properties. Generally, polymeric matrix has low strength and Young's modulus, ceramics matrix is strong, stiff and brittle, while metallic matrix is ductile with intermediate strength and Young's modulus [116].

Types of Matrix		Matrix materials	Uses
Polymeric	**Thermoset resins**	Epoxies	Principally used in aerospace, aircraft and sports goods applications
		Polyesters and vinyl esters	Principally used in automotive, marine, chemical, electrical, and consumer goods applications
		Polyurethanes and polyurea	Principally used in reaction injection molding process for manufacturing automotive body parts
		Pheonlics	used in both aerospace and automotive applications
		Bismaleimides, polyimides, polybenzimidazoles etc.	Used for high temperature aerospace application
	Thermoplastics	Nylon 6,6, Nylon 6, thermoplastic polyesters (such as PET and PBT), polycarbonate, polyacetals, polypropylene, etc	Used in discontinuous fibres in injection molded articles
		Polyether ether ketone (PEEK), polyphenylene sulfide (PPS), polysulfone (PSUL), polyamide-imide (PAI), polyether imide (PEI) etc	Used with both continuous and discontinuous fibres and moderately high temperature applications.
Metallic	Aluminum alloys, titanium alloys, magnesium alloys, copper-based alloys, nickel-based alloys		Used or moderately high temperature applications
Ceramic	Silicon carbide (SiC), aluminum oxide (Al_2O_3), silicon nitride ($Si_3 N_4$), carbon		Used for high temperature applications

Table 2-3 Matrix materials commonly used in composites [117]

Polymers are the most commonly used matrix for polymeric matrix composites (PMC) as they do not require high pressure or high temperature for processing and the problems associated with the degradation of the reinforcement are significantly less than other matrices during the manufacturing process [116].

Polymers are divided into thermoset and thermoplastics as shown in Table 2-3. Thermosets are materials that change chemically on heating [118], and the molecules are chemically jointed together by cross links forming a rigid three-dimensional network structure as shown in Figure 2-10 [32]. Thermoset polymers are brittle at room temperature having lower fracture toughness [116] and cannot be melted by heating after crosslink are formed during polymerization reactions [32]. They are more resistant to chemical attack, have better creep properties than thermoplastics and can be used at higher temperatures [116]. A list of various matrix materials commercially used is given in Table 2-3.

Over the years, the properties of epoxy have been modified by adding either rubber particles or fillers. The addition of rubber decreases its modulus and strength and increases fracture toughness while the addition of fillers improves its modulus and strength and decreases fracture toughness. The volume fraction of typical filler is as much as 10–20% which contributes to the betterment of these properties. On the other hand it makes the processing of material difficult. It also increases the density of the resin [119].

Thermoplastic materials are ductile and tougher than thermoset materials and are commonly used in nonstructural applications. Thermoplastic molecules do not crosslink hence they can be easily melted by heating and solidified by cooling. Due to their flexible and reform-able nature they can be reshaped repeatedly with ease [114].

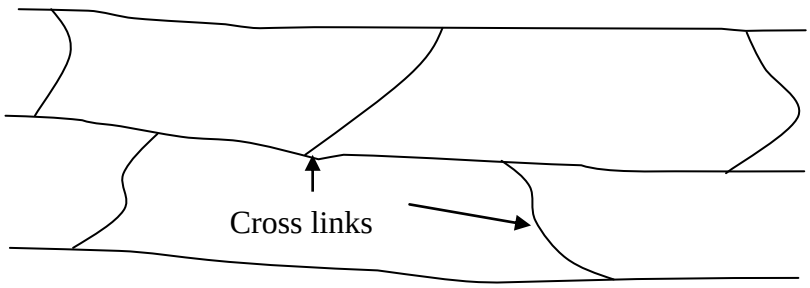

Figure 2-10 Schematic representation of thermoset polymer

2.13.4 Carbon Fibre and Epoxy Resin Composite

Carbon fibres can also be made of polyacrylonitrile (PAN) which is an acrylic textile fibre produced by wet or dry spinning of the basic polymer [120] whereas the resin is epoxy having a very good resistance to temperature [6]. The main idea in the creation of a composite is to improve the mechanical properties such as stiffness, toughness, strength and endurance against harsh environmental conditions and to prolong practical conditions [121]. Its mechanical properties can be easily tailored according to structural needs. It also has the ability to absorb kinetic energy during automobile accidents or other impact events [122]. The cost of high performance epoxies is higher but they offer good chemical and corrosion resistance [114].

CHAPTER 3. CURRENT STUDY

In this study, static and cyclic tensile loads were applied on a composite plate and the stress/strain generated was studied. This plate was made of carbon/epoxy composite with known geometrical properties. The plate was numerically simulated using the finite-element method (FEM), and its stress/strain results were then validated by comparison to experiments.

3.1 Motivation

Why?

Corrosion and heavy weight constitute a large group of issues in the use of most metallic materials such as steel and cobalt. This concern provided the motivation at present to develop new high-strength, low-density and long-lasting materials suitable for industrial and medical applications. These versatile characteristics can only be found in composite materials.

Defects in Composites

There are some common defects in composite material developed during the manufacturing process and some occur while its usage. These defects include voids, inclusions, debonds, concealed cuts, knots, lack of rovings, resin starved layers and improperly cured resin and delamination [44]. Improper design, fabrication, manufacturing and service induced damages are the factors responsible for such defects.

Methodology

In order to utilize the full potential of composite materials, a proper and extensive assessment has to be carried out to detect the defects. The defects are assessed by various methods; some resulting in complete destruction of the sample and other are nondestructive.

In the current study, the thermal imaging technique was used to determine stress distribution on the surface of a sample by nondestructive testing (NDT) using the lock-in thermographic method. The method was found to be deterministic in a tolerable level for the evaluation of stress distribution in polymer composites.

Strain gauges were also used to measure strain values at different locations on the specimen. The strain values obtained were then compared with the FEA results. These measurements were then compared to the thermography.

3.2 Research Question

For a carbon/epoxy composite rectangular plate, do the FE analysis and strain gauge experimental results agree with the stress/strains measured from lock-in thermography?

3.3 Aims and Novelty of this Study

The distinct goal of this research work is:

- To develop and validate a new platform for nondestructive testing on composite plate using lock-in thermography.

In order to complete the above goal, a series of specific objectives are required:

- Provide a brief, yet comprehensive literature on lock-in thermographic NDT technique. Advantages and disadvantages of thermographic NDT technique are also considered in the review.
- Develop a realistic finite element geometry of the sample material in Solid Works.
- Apply a numerical model of finite element analysis to the geometry of carbon/epoxy composite rectangular plate.
- Conduct an experimental study to measure strain, while applying tensile static and cyclic loads during strain gauge experiments.
- Validate FE model by comparing FEA results with the experimental strain gauge results for tensile static loading.
- Conduct an experimental study of stresses generated in the carbon/epoxy composite rectangular plate under tensile cyclic loading conditions through lock-in thermography, and comparing the results previously obtained by strain gauges.

CHAPTER 4. STRAIN GAUGES

4.1 Experimental Study, Strain Gauges

In several studies [16, 123-125], validation experiments have been done on rectangular carbon epoxy composite plates with a hole. In current study, the composite plate was subjected to average cyclic tensile loads of 1000N and 1500N and maximum static tensile loads of 1000N, 2000N and 3000N. The values of strains were measured with the help of strain gauges at four different points around the hole and at certain distance from the hole. Strain gauges gave accurate results in linear range of composite material. Strain gauge locations and specimen geometry with circular holes are shown in Figure 4-1 and Figure 4-2 respectively.

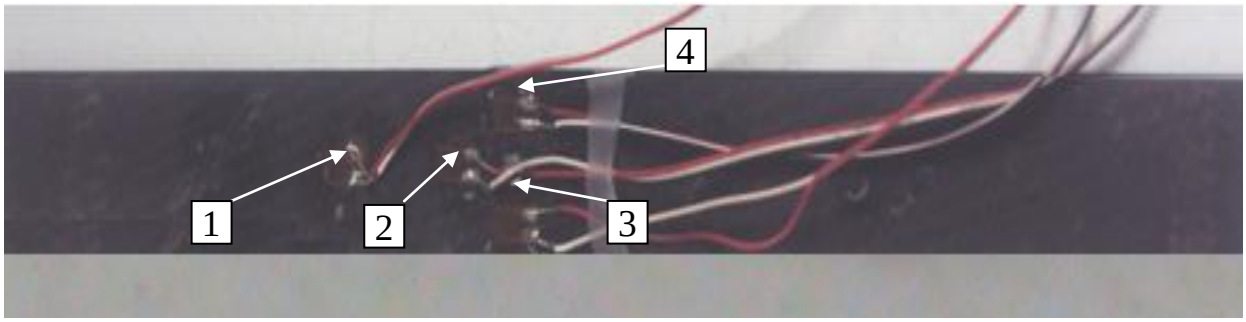

Figure 4-1 Strain gauge Locations on Composite Plate, First strain gauge was installed at a distance of 37.5 mm from the center of the hole in upward direction while the other three strain gauges were installed at the distance of 3.5 mm around the hole. A tolerance of ±0.5mm was considered for all four strain gauges.

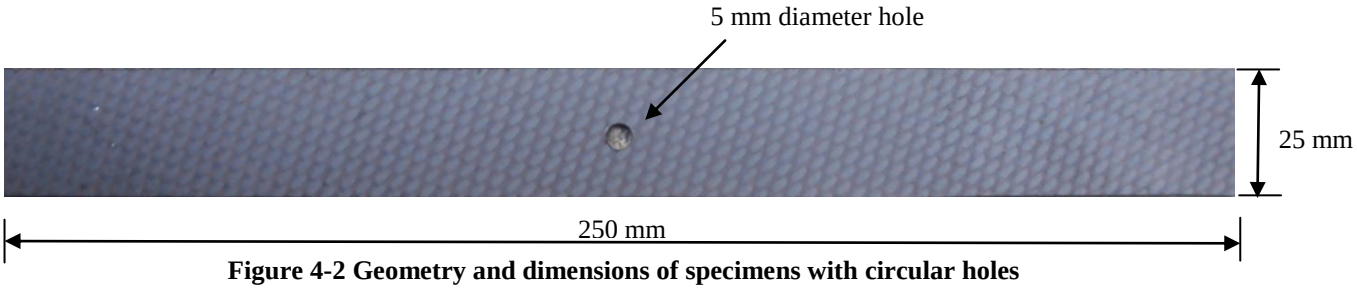

Figure 4-2 Geometry and dimensions of specimens with circular holes

The tensile tests were performed by an Instron 8874 testing machine (Instron, Norwood, MA, USA) at the Martin Orthopaedic Biomechanics Laboratory of St. Michael's Hospital (Toronto, ON, Canada).

The strain was monitored and recorded continuously during each load application. Strain gauge 1 was placed at a distance from the hole and the strain gauges at location 2, 3 and 4 were mounted around the hole.

4.2 Strain Gauge Selection

Strain gauge selection is dependent upon the problem being studied and properties of the specimen on which the gauge will be mounted. Temperature sensitivity, high strain sensitivity, and electrical resistivity of the foil are some of the important factors involved in strain gauge selection [126].

There are different sizes of strain gauges available in the market, which measure the average value of the strain gauge under the active grid area. Accuracy in the measurement of local strain concentrations increases as the size of strain gauge decreases, that is, smaller the strain gauge, better the result [16]. Strain gauge size plays an important role in proximity effect. So proximity effect should also be considered during gauge selection.

Szivek and Gharpuray [126] recommended high resistance gauges (ideally 350 Ω) due to the poor thermal conductivity of composite material [45]. In this study uniaxial gauges were considered sufficient due to the fact that the axial loading was applied on the specimen and strain was also produced in the same direction. Vishay® 350-Ohms general-purpose uniaxial linear-pattern gauges (model CEA-06-125UW-350, Vishay Micro-Measurements & SR-4, Raleigh, NC, USA) were used as shown in Figure 4-3. The detailed specifications of these gauges are given in Table 4-1 [128].

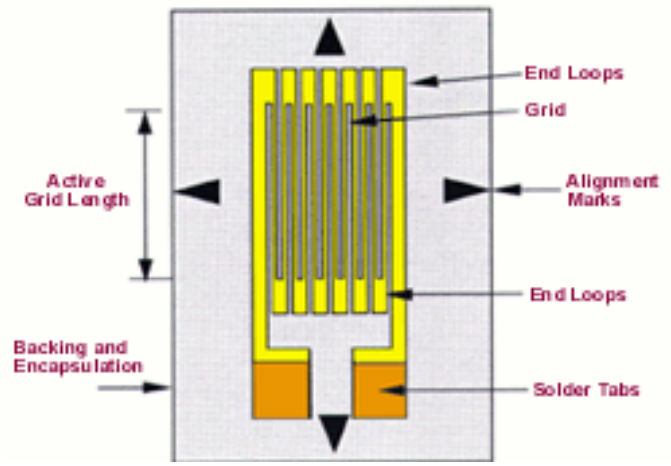

Figure 4-3 Vishay® 350-Ohms strain gauge model CEA-06-125UW-350 [127]

Model	CEA-06-125UW-350
Description	Universal general purpose strain gauges
Resistance	350.0 Ω ± 0.3%
Overall length and width	(7×11 mm)
Temperature range	-75°C to 175°C
Gauge factor, GF (at 24°C)	2.120 ± 0.5%
GF sensitivity	(1.2 ± 0.2) % /100°C
Transverse sensitivity	(0.7 ± 0.2) %

Table 4-1 Vishay® 350-Ohms strain gauge specifications [128]

4.3 Location of Strain Gauges

Figure 4-1 shows the locations of strain gauges mounted on carbon/epoxy rectangular plate. First a strain gauge was installed at a distance of 37.5 mm from the center of the hole along the plate's long axis while the other three strain gauges were installed at the distance of 3.5 mm around the hole. A tolerance of ±0.5mm was considered for all 4 strain gauges.

4.4 Strain Gauge Installation Procedure

Vishay Micro-Measurements system described the procedure for proper installation of strain gauge to get accurate results, which includes the following basic operations [129]:

- Degreasing
- Surface Abrading
- Gauge layout lines
- Conditioning
- Neutralizing
- Strain Gauge Preparation
- Strain Gauge Bonding
- Wiring and Data acquisition

4.4.1 Degreasing

The specimen surface was wiped cleaned with GC-6 Isopropyl Alcohol to remove oils, greases, organic contaminants and soluble chemical residues [129].

4.4.2 Surface Abrading

A 400-grit silicon carbide paper was used to remove dirt and dust particles from the surface of the specimen as minimal curvature may influence strain gauge results.

4.4.3 Gauge layout lines

First the position of the strain gauge was mapped on the specimen by a permanent marker. Gauge alignment was very important as 2° misalignment could lead to an error of 15 % [130].

4.4.4 Conditioning

Water-based acidic surface cleaner, namely M-Prep Conditioner from Vishay was used to clean the entire surface and to remove any remaining residues. The surface was then continuously scrubbed with cotton swab, while conditioner was applied continuously until a cleaned cotton swab was no longer discoloured. It was made sure that the cleaning solutions did not dry on the surface. The surface was then wiped dry with a single slow stroke of the gauze sponge. In order to prevent debris from coming in from the boundary, the stroke began inside the clean area.

4.4.5 Neutralizing

Vishay Micro-Measurements strain gauge adhesive systems works best when pH value is between 7.0 and 7.5 [129]. The residual M-Prep Conditioner on the surface was then neutralized by applying M-Prep Neutralizer 5A to the cleaned surface and scrubbing with clean cotton-swab until the whole surface was neutralized. The surface was then dried by wiping in the same manner as done in Section 4.4.4.

4.4.6 Strain Gauge Preparation

The strain gauge was taken out of the package carefully. The strain gauge received from Vishay Micro-Measurements was chemically cleaned, and for good adhesion the underside was treated specially [129]. The outside of the gauge was adhered to PCT-2A cellophane tape such that when the tape was applied on the specimen the inside of the gauge came in contact with the surface.

M-Bond 200 Catalyst was applied to the inside of the gauge and left to dry for at least 30 seconds.

4.4.7 Strain Gauge Bonding

M-Bond 200 was applied on the bonding side of the gauge and the cellophane tape was flipped. The tape was then carefully applied to the specimen by placing the gauge at exact location as marked before in Section 4.4.3. The cellophane tape was pressed firmly with sterilized cotton to remove any air bubbles between the gauge and plate surface, until the wiring was performed. The other three strain gauges were attached to the specimen as described above in Section 4.4.6 and 4.4.7.

4.4.8 Wiring and Data Acquisition

Colour-coded red, black and white lead wires were used in this experiment and were connected to the +VB1, I1_1/4B1 and IN1 slots, respectively, of DSub-15-Pin Connector (ACC/DSUB-UNI2, IMC Mess-System GmbH, Berlin, Germany). A loop was made between the IN1 and SENSE1 slot. Figure 4-4 shows the completed circuit of Quarter Bridge of the strain gauge.

The second strain gauge was connected to the same connector except red wire was connected to the +VB2 slot. Two strain gauges were connected to one connector. For this study two DSub-15-pin connectors were required to properly wire all 4 strain gauges.

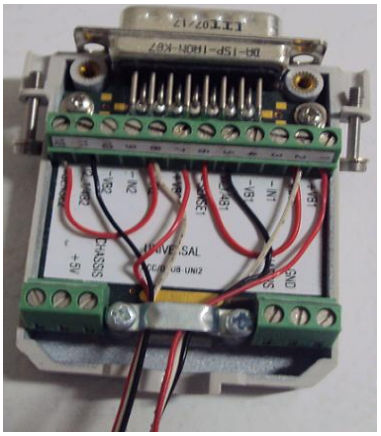

Figure 4-4 Two-Channel DSub-15-Pin Connector attached to Wiring from Two Strain Gauges

The other end of all three wires was stripped off, and the red wire was soldered on the right terminal of the gauge and the other two were soldered on the left terminal. Hence a three wire

quarter-bridge circuit was wired as per manufacturer's instruction [129] as shown in Figure 4-5 and Figure 4-6.

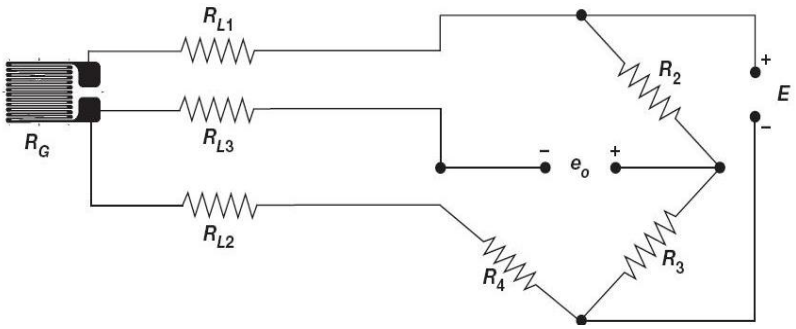

Figure 4-5 Three-wire quarter-bridge circuit [131]

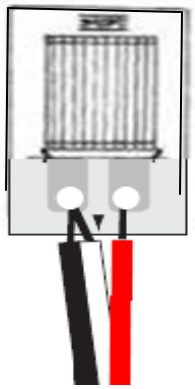

Figure 4-6 Soldering illustration of three Lead Wire Conductors to a Strain Gauge [132]

Once all 4 gauges were connected to DSub-15-pin connectors, they were plugged into a data acquisition unit CRONOS-PL2 (IMC Mess-Systeme GmbH, Berlin, Germany) as shown in Figure 4-7, through a UNI2-8 eight-channel all-purpose amplifier as shown in Figure 4-8.

The CRONOS-PL2 was then connected to a data collection laptop computer installed with signal analysis software FAMOS V5.0 (IMC Mess-Systeme GmbH, Berlin, Germany).

Figure 4-7 DSub-15s Connected to the CRONOS-PL Unit

A potiental difference of 5 Volts was applied to the quarter bridge option when the strain gauge setting in FAMOS V5.0 was configured. FAMOS V5.0 had a built-in option which was used to balance all strain gauge circuits. The readings in microstrains from all the strain gauges were plotted against time.

Figure 4-8 UNI2-8, all-purpose eight-channel amplifier

4.5 Sensitivity of Strain Gauge

Gauge factor (GF) is a fundamental parameter defining the sensitivity of the gauge to the strain. It is the ratio between fractional changes in electrical resistance and fractional change in length (i.e. strain) as shown in equation 6

$$GF = \frac{\Delta R / R_G}{\Delta L / L} = \frac{\Delta R / R_G}{\varepsilon} \quad \text{..... Equation 6}$$

where ΔR is change in gauge resistance, R_G is gauge resistance, ΔL is relative change in gauge length, L is absolute gauge length and ε is the strain.

The resistance of the strain gauge would change when subjected to applied strain in ideal condition but practically the gauge and the specimen would also respond to change in temperature. The sensitivity of a strain gauge to temperature was minimized during its manufacturing process to compensate thermal expansion of the specimen material. Measurements of strain were usually done in order of a few millistrain that produced very small changes in resistance which must be measured accurately. Small amplification of strain sensitivity provided by GF is not sufficient for measurement. For example, a microstrain of 1000

(microstrain, $\varepsilon \times 10^{-6}$) measured by a strain gauge with a GF of 2 would show electrical resistance of $2 \times (1000 \times 10^{-6}) = 0.2\%$. It means that the change will only be 0.7 Ω for a 350 Ω gauge. Wheatstone bridge configuration of the strain gauges with a voltage or current excitation source was used to measure small resistance change and to compensate temperature sensitivity [133].

4.6 Strain Gauge Experimental Summary

In this study, the specimen was subjected to static (maximum forces, 1000N, 2000N, and 3000N) and sinusoidal cyclic tensile loads (average forces, 1000N and 1500N) (Figure 4-9). A hydraulically powered Instron® 8874 (Instron, Norwood, MA, USA) (Figure 4-10) was used for axial load application. The load cell of the machine had a capacity of ±25 kN, a resolution of 0.1 N and an accuracy of ±0.5%. The Instron's loading frame had a linear stiffness of 260 kN/mm, which was far greater than what was expected for the composite plates to be tested. Thus, no calculation was deemed necessary to compensate for Instron tester compliance.

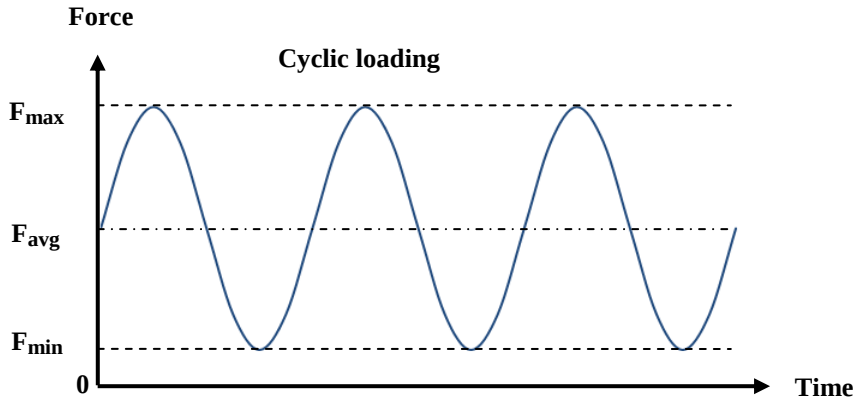

Figure 4-9 Cyclic loading application on carbon epoxy rectangular plate

A desktop computer running the interface software FastTrack™ 2 provided the tensile loading rate and maximum load to the specimen through FastTrack™ 8800 servohydraulic controller unit (Instron, Norwood, MA, USA) as shown in Figure 4-11.

The LAN network connected the CRONOS-PL unit to the data collection computer running the signal analysis software FAMOS V5.0 (IMC Mess-Systeme GmbH, Berlin, Germany). The gauge factor and resistance were set to 2.12 and 350 Ω respectively as per manufacturer's specifications [134]. A 100N linear preload was applied to avoid slippage between the composite plate and loading cell fixture and to settle any prevailing micro-motion in the specimen plate.

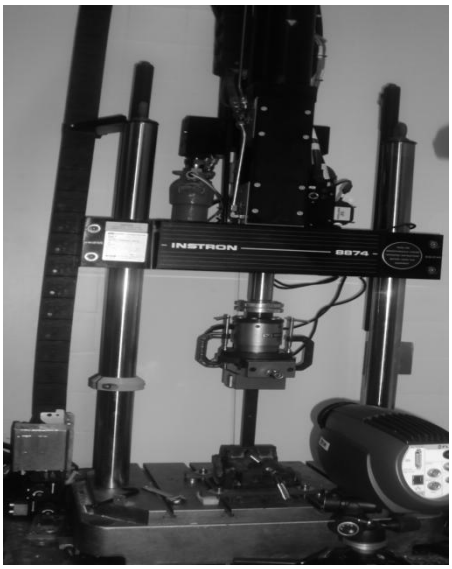

Figure 4-10 Instron® FastTrack™ 8874

The active area of the strain gauges gave the average value of strain [16, 125] which was displayed in microstrain (με) and plotted against time. The test was performed and measured three times for each load and the average values were recorded and used for analysis.

Figure 4-11 Instron® FastTrack™ 8800 Controller Panel

CHAPTER 5. LOCK-IN THERMOGRAPHY EXPERIMENTS

Infrared thermography, a kind of NDT technique, was used for the carbon/epoxy composite plate to measure the surface temperature of the specimen and to analyse the heat flow pattern. The subsurface flaws detection in carbon-epoxy composite materials was carried out effectively by lock-in thermography [135].

5.1 Experimental Setup for the Current Study

In this study, a composite plate was subjected to mechanical loading which induced a thermal effect for nondestructive characterization on short term excitation. The internal heat generation in the specimen due to mechanical loading was the microstructure characteristic, which correlated with the material property of the specimen.

The current setup for the study was comprised of a target, a thermal camera (model FLIR Silver 420, Burlington, ON, Canada), a PC-based image acquisition system (a laptop computer) and a function generator. The target was a rectangular plate made of carbon epoxy composite with an emissivity of 1 and a coefficient of thermal expansion of $2.6 \times 10^{-6}/^{0}C$.

The components of the thermal camera consisted of an optical receiver and a detector. Every element of the camera divided the signal into optical, electronic and electromagnetic noise for which a data processing step was required.

The Instron 8874 mechanical tester supplied a cyclic load to the specimen which was synchronized with the IR camera. The specimen was clamped up to 30 mm from the both ends in the upper and lower jaws of the Instron machine, and the upper jaw connected to the actuator supplied the load. The cyclic average loads of 1000N and 1500N were applied to the specimen at the frequency of 5 Hz. The IR camera was fixed on a tripod and placed at a distance of 1m from the specimen (as shown in Figure 5-1) in order to capture stable images without any vibration. After the images were captured by the camera, the actuator lifted and released the load on the specimen.

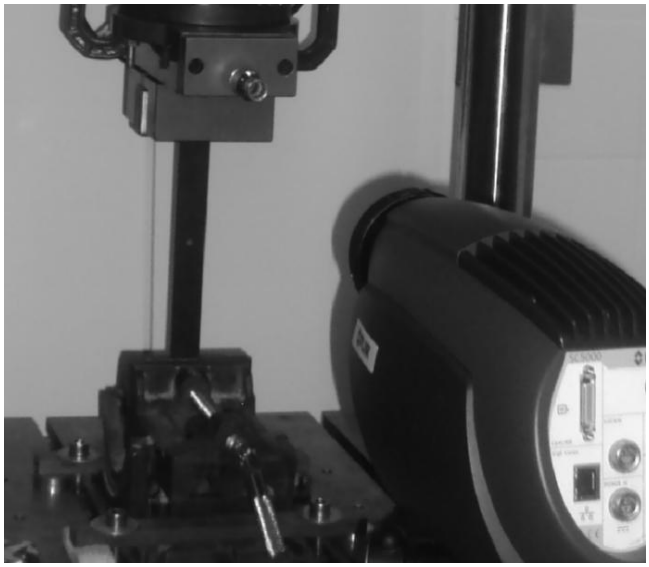

Figure 5-1 Infrared experimental setup

IR camera was used to record the surface temperature of the specimen by taking the infrared signals. The system synchronized these IR signals with the loading signals (Figure 5 2). Lock-in system of the camera acquired four signal values (Figure 5-2) in every pixel of the image. Then from these signal values the system calculated a phase value (Φ) according to the following equation

$$\Phi = \arctan\left(\frac{S_1 - S_3}{S_2 - S_4}\right) \text{..... Equation 7}$$

Using the phase values calculated with equation 7, the system produced a phase image. By assuming adiabatic conditions, Altair software of the camera conducted thermo-elastic stress analysis from the equation given by Lord Kelvin as below:

$$\Delta T = T \frac{\alpha}{\rho C_p} \Delta\sigma \text{ ..... Equation 8}$$

where ΔT is change in the temperature, T is ambient temperature, α is the coefficient of thermal expansion, ρ is the density, C_p is the specific heat capacity, and $\Delta\sigma$ is change in the stress. Then the stress measurement plots were generated by Altair software and saved for further analysis.

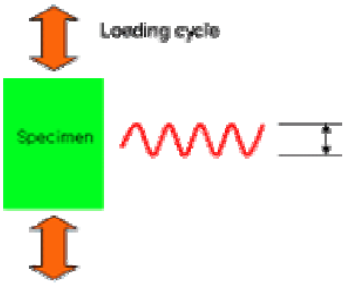

(a) Loading cycle

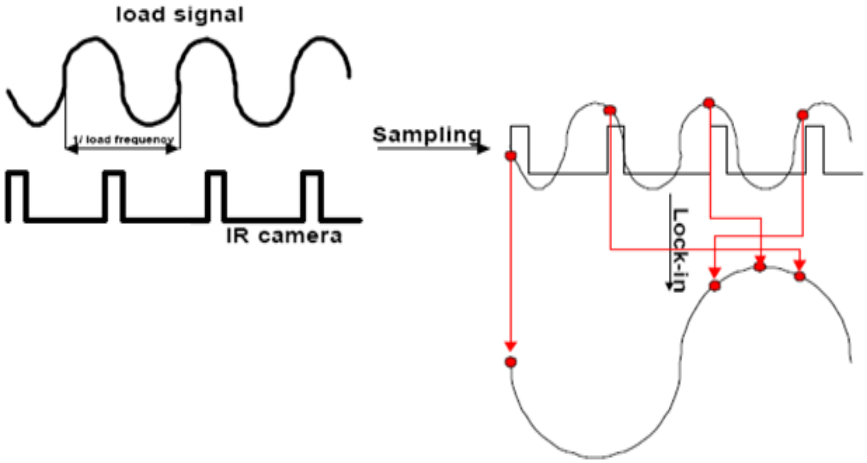

(b) Signal processing in thermal stress

Figure 5-2 Lock-in Thermography process [24]

5.1.1 Description of Thermal Camera Used in the Current Study

The thermal camera called Silver 420 camera, used in this study, carried out thermal measurements with the greatest sensitivity, precision and speed. The thermal resolution of the infrared camera was 0.1 °C and could work at 0 °C. It captured thermal images at 60 frames per second with a wave length of 2.5-5.1 μm. The scanner and the detector of the camera were very sensitive with 320 x 256 pixels while keeping an extraordinary dynamic range and perfect linearity [136].

This thermal camera was equipped with integrated motorized lens and could be easily focused by using the control button in software. The object must be located at the centre of the image and focused properly before taking measurement. A BNC 75 ohms cable connected camera with the video monitor provided with the camera.

Characteristic of the Silver 420 camera are presented in the Table 5-1:

Parameter	Values
Spectral Response (wave length)	2.5 µm – 5.1 µm
Frame Rate	5 Hz to 170 Hz full Frame
Image Capture	Snapshot Integrate then Read mode (ITR)
Number of Pixels	320 x 256 pixels
Pitch size	30 µ m x 30 µm
Digital video	USB / Cam LINK
Analog Video	PAL (50 Hz) or NTSC (60 Hz)

Table 5-1 Technical date of Silver 420 Camera [137]

CHAPTER 6. FINITE ELEMENT ANALYSIS

6.1 Background of Finite Element Analysis

Finite element method (FEM) is used for calculating complex engineering system. It calculates and analyzes static and dynamic conditions applied on complex and irregular shaped bodies [122]. FEM is a totally computerized method which uses sophisticated software, desktop hardware and can be used easily with accurate results. The principle of FEM is to replace the actual continuous structure by mathematical model by dividing it into finite size elements of known elastic and inertia properties.

6.2 Geometric Modelling of Composite Plate

A scaled solid model of the CFRP plate was developed with the help of CAD software Solid Works® 2009 (Solid Works Corporation, Dassault Systèmes, Concord, MA, USA). The geometry of rectangular plate was then saved as a Parasolid Binary format (*.x_b; Siemens PLM Software, Siemens AG, Berlin and Munich, Germany) as it was compatible with ANSYS software. The geometry in Parasoild Binary format was exported to ANSYS Design Modeler which was used in Simulation window of ANSYS Workbench 11.0 (ANSYS, Inc., Canonsburg, PA, USA).

6.2.1 Geometry of Carbon Fibre Reinforced Epoxy Composite

The plate used in this study was made of carbon fibre reinforced epoxy composite having a regular surface of rectangular cross section. The dimensions of the specimen are, thickness T = 2.2 mm, length L = 250 mm and width B = 25 mm, each layer is 0.37 mm thick with a circular drilled hole of 5mm diameter in the centre. The global coordinate system is shown in Figure 6-1.

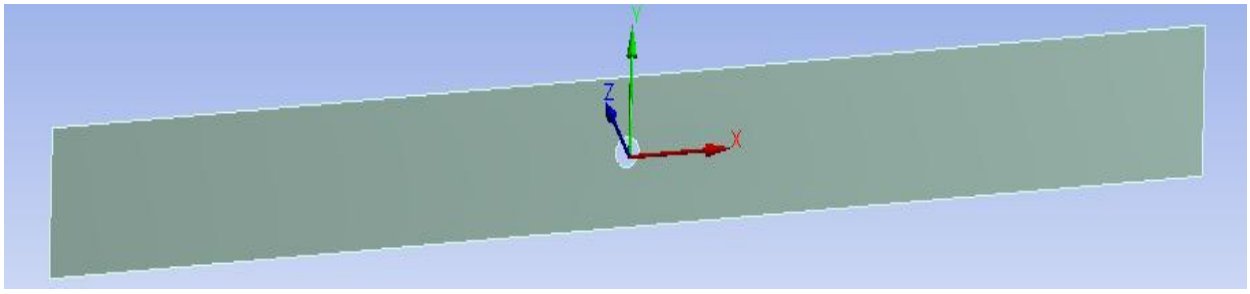

Figure 6-1 Carbon epoxy composite rectangular plate

6.3 Material Properties

The properties of the carbon epoxy composite are shown in the Table 6-1.

Properties	Values
Modulus of elasticity, E_{11} (GPa)	51.8 ± 0.43
Modulus of elasticity, E_{22} (GPa)	49.3 ± 0.37
Modulus of elasticity, E_{33} (GPa)	11.5 ± 0.13
Shear modulus, G_{12} (GPa)	3.24 ± 0.15
Shear modulus, G_{13} (GPa)	3.55 ± 0.07
Shear modulus, G_{23} (GPa)	3.47 ± 0.19
Poisson's ratio, v_{12}	0.065 ± 0.001
Poisson's ratio, v_{13}	0.48 ± 0.008
Poisson's ratio, v_{23}	0.49 ± 0.007
Fibre volume fraction (V_f) %	53
Matrix volume fraction (V_m) %	47
Density (g/cm^3)	1.44
Ply orientation	± 45°

Table 6-1 Elastic properties of Carbon fibres/epoxy resin [6, 122, 138-141]

6.4 Simulation Using ANSYS

ANSYS workbench ver. 11 was used to perform Finite Element analysis (FEA) in its simulation window. Linear elastic condition and orthotropic material properties were considered during analytical calculations of FE. Vertical axial tensile loads of 1000N, 2000N, 3000N were applied consecutively at one face of the plate with no contact surfaces.

6.4.1 Boundary Conditions

The boundary conditions were applied on the plate in a manner that movement of all nodes on one side was restricted along the axis of symmetry as shown in Figure 6-2. The specimen was placed in a fixed support at one end shown as dark blue marker in Figure 6-2 and three different

loading conditions were applied at the other end of the plate. This type of arrangement provided a practical simulation to the gripping conditions applied during testing.

Figure 6-2 Boundary conditions on the assembly, Force direction is indicated by the red arrow.

6.5 Mesh Sensitivity and Convergence

Under the same applied load, the response of a series of meshes of increasing refinement was studied in order to test the mesh sensitivity in the geometry of carbon epoxy plate with 5mm hole diameter. Four vertices were selected on FEA model corresponding to the strain gauge locations. "Relevance", a global mesh control utility, was used to perform refinement in ANSYS Workbench. The relevance ranges from high speed mesh (-100) to high accuracy (+100). For each loading condition 5 meshes were created by changing the relevance settings and tested for the composite plate as shown in, Figure 6-3. The strains and nodes were recorded after each refinement until the data converged adequately.

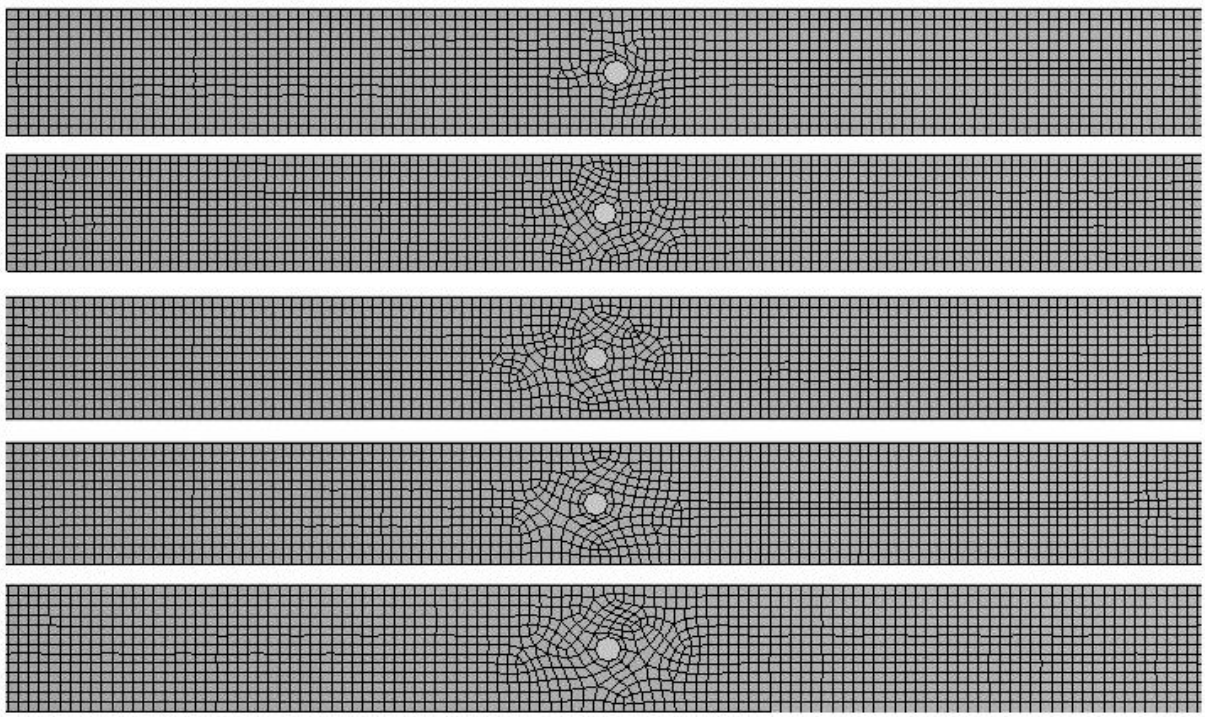

Figure 6-3 From top to bottom, mesh relevance, 100, 80, 60, 40 and 20% for the Composite plate

The mesh characteristics, nodes and associated microstrain values are tabulated in Table 6-2 for different meshes and difference in percentage from preceding mesh is given within brackets.

Load	Relevance	Nodes	Solid Elements	Format: Corresponding value (%difference from previous value) Normal Stress (MPa)			
				G1	G2	G3	G4
1000N	20	1613	1760	364.90	550.56	742.40	751.61
	40	1619	1755	348.67(4.45)	827.12(50.23)	842.70(13.51)	888.56(18.22)
	60	1735	1625	334.14(4.35)	557.50(32.60)	951.80(12.95)	982.90(5.03)
	80	1749	1609	345.02(3.26)	894.21(60.40)	917.52(3.60)	1032.3(5.03)
	100	1765	1620	354.24(2.67)	915.89(2.42)	952.49(3.81)	991.06(3.99)
2000N	20	1613	1760	710.64	920.96	1520.30	1393.10
	40	1619	1755	695.54(2.12)	1361.60(47.85)	1817.20(19.53)	1839.40(32.04)
	60	1735	1625	664.94(4.40)	667.19(51.00)	1917.30(5.81)	1935.70(5.24)
	80	1749	1609	662.570.36)	1547.1(131.88)	1934.7(0.91)	1819.9(5.98)
	100	1765	1620	679.06(2.49)	1968.00(27.21)	1965.70(1.60)	1867.00(2.59)
3000N	20	1613	1760	1067.70	1408.20	2107.20	2078.90
	40	1619	1755	1762.20(65.05)	2390.20(67.73)	2912.60(38.22)	3067.30(47.54)
	60	1735	1625	980.81(44.34)	2410.40(0.80)	3069.50(5.39)	3185.10(3.84)
	80	1749	1609	995.7(1.52)	2752.5(14.19)	3339(8.78)	3342.8(4.95)
	100	1765	1620	1001.70(0.60)	3017.50(9.62)	3568.70(6.88)	3485.80(4.28)

Table 6-2 Number of Nodes and elements of different meshes for various relevance

After examining all the results of meshing relevance it was concluded that the mesh having 100 relevance was the best fit for this study, since an increase in the number of nodes to mesh of 100 relevance provided only marginal change in strain values for all locations.

CHAPTER 7. RESULTS AND DISCUSSION

7.1 Experimental and FEA Results

7.1.1 Strain Gauge Test Results (Static Loading)

The carbon epoxy composite plate was instrumented to measure strain values at 4 locations. The specimen was tested for maximum static tensile loads of 1000N, 2000N, and 3000N. The strain values measured from strain gauge experiment are tabulated in Table 7-1. All locations under investigation experience tension. It is evident that the values of strain increase as the load increases as shown in Figure A1-1 of Appendix 1.

Gauge location	**Measured strain (με) from experiment**			**State of load experienced**
	1000N	2000N	3000N	
1	1254	1816	3885	Tension
2	962	1943	3411	Tension
3	907	1979	3575	Tension
4	925	1897	3516	Tension

Table 7-1 Experimentally measured microstrain values in tensile static loading

7.1.2 Surface Strains values from FEA (Static Loading)

Calculated microstrains due to maximum tensile static loads of 1000N, 2000N and 3000N are tabulated in Table 7-2, these locations correspond to experimental strain gauge locations. The strain values follow the same trend as observed during the strain gauge experiment.

Location	Calculated strain (με) from FEA			State of Load Experienced
	1000N	2000N	3000N	
1	354.24	679.06	1001.70	Tension
2	915.89	1968.00	3397.50	Tension
3	952.49	1965.70	3568.70	Tension
4	901.06	1867.00	3485.80	Tension

Table 7-2 Microstrain values calculated from FEA

7.1.3 Strain Gauge Test Results (Cyclic Loading)

The results of strain from average cyclic tensile loads of 1000N and 1500N are given in Table 7-3. The specimen experiences tension at all strain gauge locations. The graphical representation of all values is shown in Figure A1-3.

Gauge Location	Measured strain (με) from Experiment		State of Load Experienced
	1000N	1500N	
1	1368	1814	Tension
2	1067	1567	Tension
3	970	1509	Tension
4	978	1523	Tension

Table 7-3 Measured microstrain values for tensile cyclic loading

The stresses were calculated using Hooke's law by taking the value of modulus of elasticity as 51.80 GPa and tabulated the results in Table 7-4.

Location	Stress (MPa) calculated from Strain gauge experiment	
	1000N	1500N
1	68.40	90.70
2	53.35	78.38
3	48.50	75.48
4	48.90	76.15
$Stress = Strain \times Young's\ Modulus$		

Table 7-4 Stress values calculated from strain gauge experiment

7.1.4 Lock-in Thermographic Test Results (Cyclic Loading)

The values of stress measured by the thermal camera when subjected to average tensile cyclic loads of 1000N and 1500N are given in Table 7-5. It is evident that the values of stress around the hole are similar, while the location far from the hole edge experiences higher value of stress.

Location	Stress (MPa) measured from LT experiment	
	1000N	1500N
1	61.43	86.77
2	52.81	70.06
3	52.93	83.48
4	54.43	84.41

Table 7-5 Stress values from LT experiment for 1000 N and 1500 N cyclic loading

7.2 Analysis of Current Study

7.2.1 Analysis of Experimental and FEA Strain Measurements (Static Loading)

The analysis of the results obtained in Section 7.1 was done in two stages. In the first stage, static tensile loads were considered and the values of strain from the FEA and the strain gauge experiments were tabulated for comparison.

The strain values obtained from the strain gauge experiment were compared to the strain values calculated by FEA to verify if the strain gauge experiment could be used to predict the strain distribution in the composite plate. Three of the four gauge readings from the experimental results agreed well with the FEA calculated results and their strain values were relatively close (within 5% difference). The reading for the strain gauge at location "1" was in high disagreement with the FEA calculated strain value as shown in Table 7-6. This disagreement of more than 70% was due to the strain gauge being located nearest to the loading cell. Strain gauges were installed with great care; however slight misalignment might lead to higher variations in the strain results.

Load (N)	**Strain Gauge Locations**											
	G1			**G2**			**G3**			**G4**		
	Normal Elastic Strain Readings (με)											
	FEA	Strain Gauge	%	FEA	Strain Gauge	%	FEA	Strain Gauge	%	FEA	Strain Gauge	%
1000	354.24	1254	71.75	915.89	962	4.79	952.49	907	5.02	901.06	925	2.59
2000	679.06	1816	62.61	1968.00	1943	1.29	1965.70	1979	0.68	1867.00	1897	1.58
3000	1001.70	3885	74.22	3397.50	3411	0.40	3568.70	3575	0.67	3485.80	3516	0.86

$$\%\ Difference = \frac{(\text{Experimental Strain Values - FEA Strain Values}) \times 100}{(\text{Experimental Strain Values})}$$

Table 7-6 Comparison of FEA and experimental Strain values for static loading

The correlation graph of all strain values excluding location 1 for all load conditions is given in Figure 7-1. The slope of correlation graph indicates that although the strain gauge experimental values has an overall tendency to overestimate the strain, there is a reasonably strong correlation between the data as exhibited by the $R^2 = 0.99$. There was a nominal experimental 'offset' strain value due to experimental preload, which corresponded to the zero FE strain.

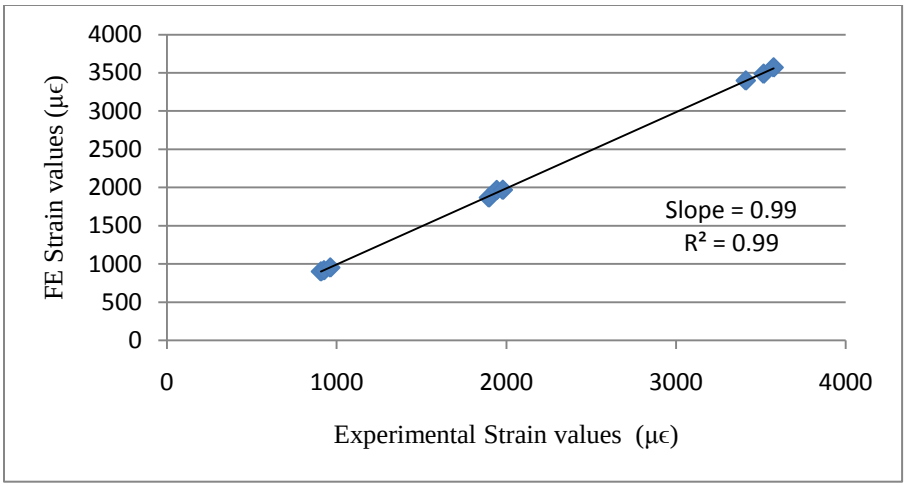

Figure 7-1 Correlation of all Strain values (excluding location 1) from FEA and Experimental results

7.2.2 Analysis of LT and Strain Gauge Experimental Measurements (Cyclic Loading)

In second stage, tensile cyclic loads were applied and the values of stress from lock-in thermography were compared with the stress values calculated from the strain gauge experimental study.

During strain gauge experimental study, cyclic tensile loads of 1000N and 1500N were applied on the specimen. The stress values were converted using Hooke's law and tabulated in Table 7-4. Stresses from experimental strain gauge and lock-in thermography were compared as shown in Table 7-7. The results from two experimental studies differed by 12% maximum.

All the stress results of lock-in thermography and the strain gauge experiment for 1000N and 1500N are complied and compared in Table A3-1 and Table A3-2 of Appendix 3, respectively. These values are plotted along separate axes in a correlation graph and R^2 values are recorded as shown in Figure 7-2. A slope of greater than 1 indicates that the strain gauge experiment overestimated the stress values, whereas a slope of less than 1 indicates that the strain gauge experiment underestimated the stress values when compared to the IR experimental results. The R^2 values are an indication of the deviation in the values of the experimental studies. A linear best fit line with a slope of 1 and R^2 value of 1 would represent the case where the stress results predicted by the strain gauge experiment exactly matched the lock-in thermographic experimental results. The correlation plot indicates that the experimental values of both studies are comparable and there is reasonably strong correlation between the data as exhibited by the R^2 = 0.87, as shown in Figure 7-2.

Load	Locations											
	G1			G2			G3			G4		
	Stress Values from LT	Calculated stress values from strain gauge readings	%	LT Experimental Stress Values	Calculated stress values from strain gauge readings	%	LT Experimental Stress Values	Calculated stress values from strain gauge readings	%	LT Experimental Stress Values	Calculated stress values from strain gauge readings	%
1000N	61.43	68.40	11.35	52.81	53.35	1.02	52.93	48.50	8.37	54.43	48.90	10.16
1500N	86.77	90.70	4.53	70.06	78.38	11.88	83.48	75.48	9.58	84.41	76.15	9.79

$$\%\,Difference = \frac{(\text{Calculated Stress Values - LT Stress Values})}{\text{Calculated Stress Values}} \times 100$$

Table 7-7 Comparison of stress values obtained from lock-in thermography and Strain gauge

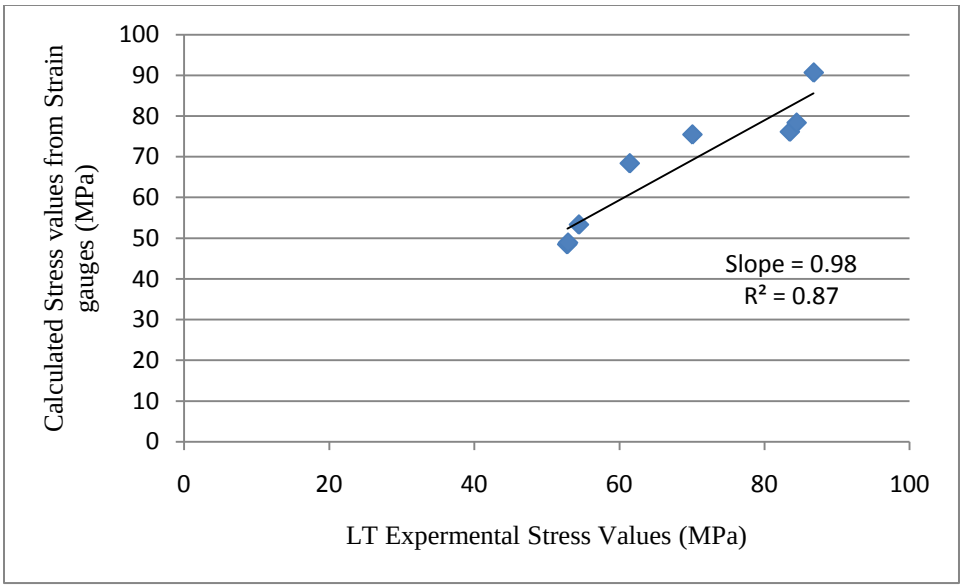

Figure 7-2 Correlation graph of stress values for all IR and experimental data

7.2.3 Analysis of Lock-in Thermographic Stress Maps using Cyclic Loading

Normal stress images were generated by Altair's software and are given in Figure 7-3 and Figure 7-4. On the x-axis (Figure 7-6) the value of stress increased by 51 % as it approached the hole. This increased stress was due to contraction resulting from tensile force acting in the perpendicular direction. The trend showed a decrease in stress by 50 % from the hole to the edge of the specimen in the x-direction for 1000 N load, as shown in Figure 7-3.

The same trend was observed for 1500N. On the x-axis, the values of stress increased from 11.26 MPa to 102.08 MPa from the edge to the hole and decreased from 102.95 MPa to 12.25 MPa from the hole to the edge of the specimen as shown in Figure 7-4.

As the load increased, the stress concentration also increased resulting in an increase of probability of damage around the hole. The stress concentration observed in the lock-in thermographic images was similar to that of the finite element analysis (as shown in Figure A2-1, Figure A2-2 and Figure A2-3) which confirmed and validated the process of lock-in thermography for detection of stress distribution. From these thermal images, it was evident that the area around the hole was the weakest part of the plate due to the stress concentration.

Variations in line 1 and 2 for 1000N and 1500N loading cases might be due to the non uniformity in the internal microstructure of the composite plate.

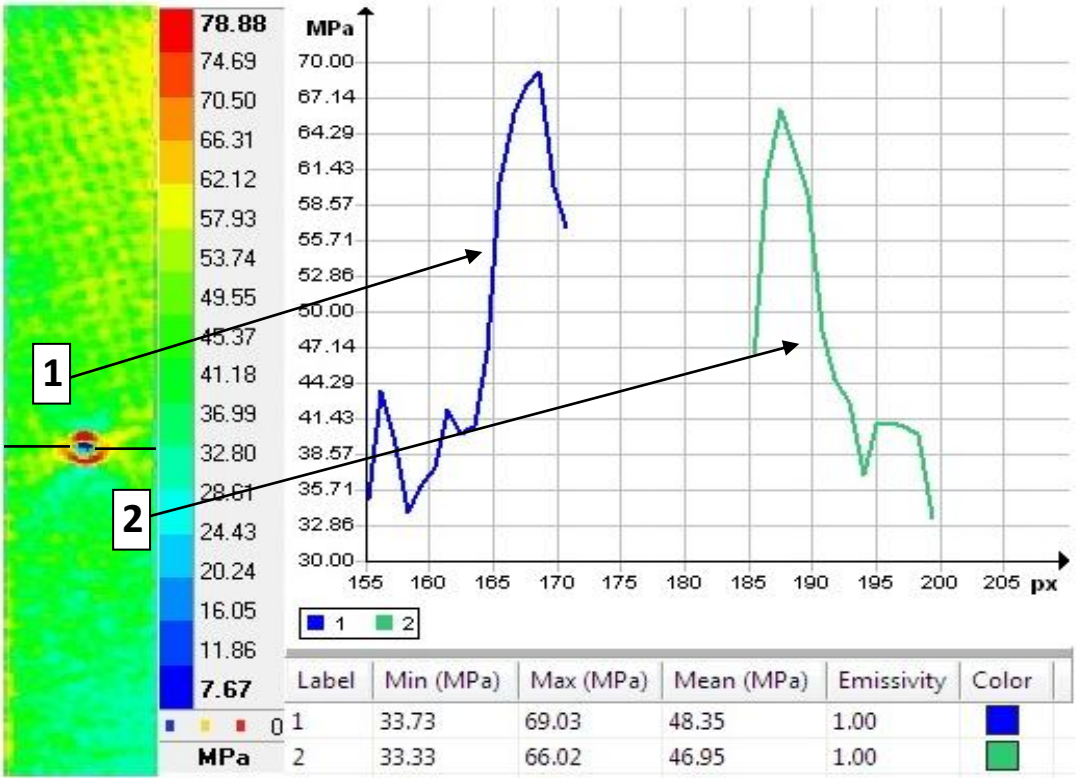

Label	Min (MPa)	Max (MPa)	Mean (MPa)	Emissivity	Color
1	33.73	69.03	48.35	1.00	
2	33.33	66.02	46.95	1.00	

Figure 7-3 Stresses along line 1 and 2 are shown in the graph for average 1000N cyclic tensile load

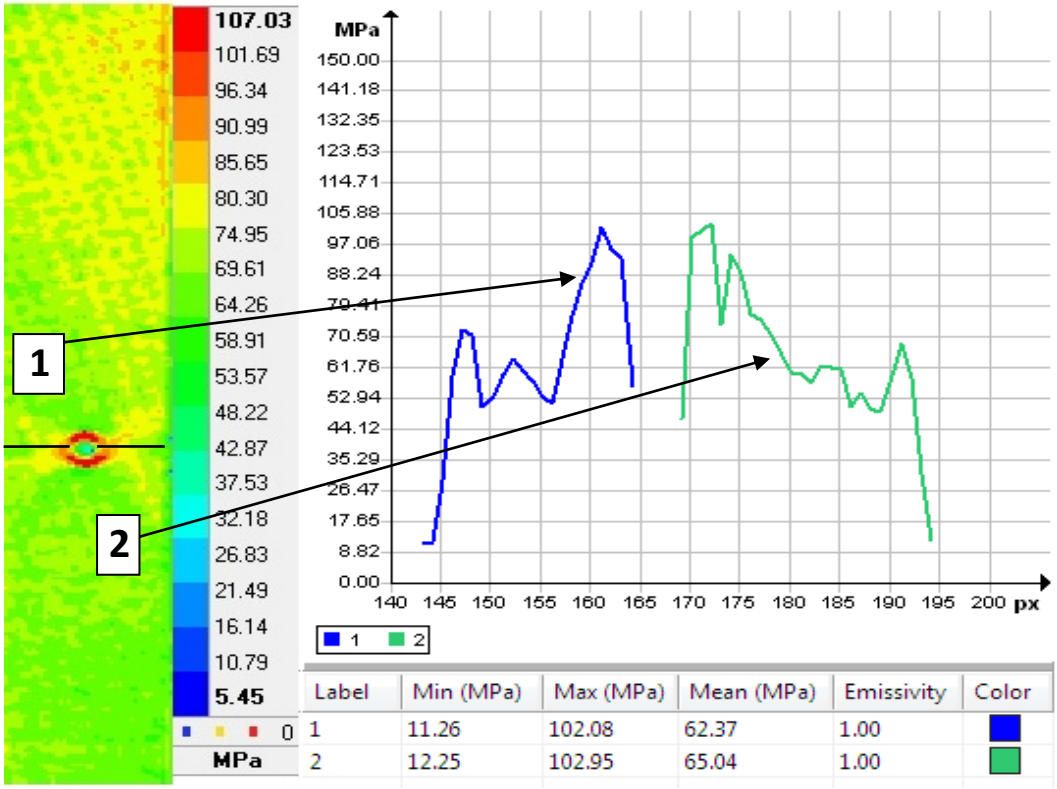

Label	Min (MPa)	Max (MPa)	Mean (MPa)	Emissivity	Color
1	11.26	102.08	62.37	1.00	
2	12.25	102.95	65.04	1.00	

Figure 7-4 Stresses along line 1 and 2 are shown in the graph for average 1500N cyclic tensile load

7.3 Discussion

7.3.1 Current Study

Three different studies were conducted to identify stress/strain distribution for tensile static and cyclic loading. The results showed strong agreement between the FEA/strain gauge and strain gauge/lock-in thermography results. In general, the lock-in thermography was able to accurately predict the observed stresses in the carbon epoxy composite plate. Unlike strain gauge experiments, lock-in thermographic experiments produced full stress maps. Even though, FEA provides full stress maps like lock-in thermography, however, it fails to captures the zones of high stresses, especially the ones close to the grips.

7.3.2 Strain Gauge Experiment versus FEA

Strain values at locations 2, 3 and 4 strongly agreed with FEA strain results within the percentage difference of 5% for 1000N, 2000N and 3000N loading cases. Recall that a slope of greater than 1 showed that FEA strain values overestimated the strain values when compared to the experimental strain results and if the slope of the best fit line is less than 1, then the model tended to underestimate the observed results. This was shown in the slope of the best fit line from Figure 7-1 which had the value of 0.99, so it meant that the FEA values underestimated the strain.

For all load cases the strain gauge at location 1 showed a higher percentage difference of 70 % (average) when both techniques were compared. This was most likely due to unstable gauge readings, as this location was close to the loading cell, such that it experienced high tensile load as compared to the locations far from the loading cell.

A careful attempt was made to ensure that all strain gauges were oriented along the vertical axis. The strain gauge orientation on the surface plane, however carefully applied, might still slightly be off-axis with respect to the vertical axis and therefore strain gauge location 1 showed a higher percentage difference. A 2° misalignment could lead to an error of 15 % (as stated in Section 4.4.3).

Therefore, the strain gauge experiment could be used to measure the strain on the specimen.

7.3.3 Strain Gauge versus Lock-in Thermographic Experiments

In general, the stress values calculated from strain gauge experiments tended to underestimate the stress values. This was shown in the slope of the correlation graph which had a value of 0.98 as shown in Figure 7-2. There was also a strong correlation with the observed data of the two experimental methods as exhibited by $R^2 = 0.87$.

The force displacement graphs for the applied loads of 1000N and 1500N, as shown in Figure A1- 5 and Figure A1- 6, indicated that the specimen remained within the linear elastic limit. No permanent damage occurred during the mechanical testing. Thus, the lock-in thermography method could reliably predict the stress values along the specimen within the linear elastic limit.

7.4 Comparing the FEA Results with the Literature

Kreculj [122] studied the effect of stress on carbon/epoxy composite material (length = 155mm, width = 25 mm, thickness = 0.13 mm) under applied tensile force. The finite element method was used to predict the stresses in the plate. The result showed that the model failed when a force of 4794N was applied. In the current study, a 3000N maximum force was applied and no failure occurred. This also showed the plate remained within the elastic limit. Hence a direct comparison to the prior study could not be possible.

Toubal *et al*. [142] used the finite element method to examine a composite plate with a circular hole in the centre to find the stress distribution. The plate was simulated and subjected to tensile loading from both ends. The specimen (E = 51 GPa) was subjected to tensile forces in the experiment. The results obtained from FEA and experimental studies were compared. Comparing Figure 7-5 and Figure 7-6 it was observed that the stress concentration area was around the hole in both studies and stress magnitude decreased as the distance between the hole and the edge increased.

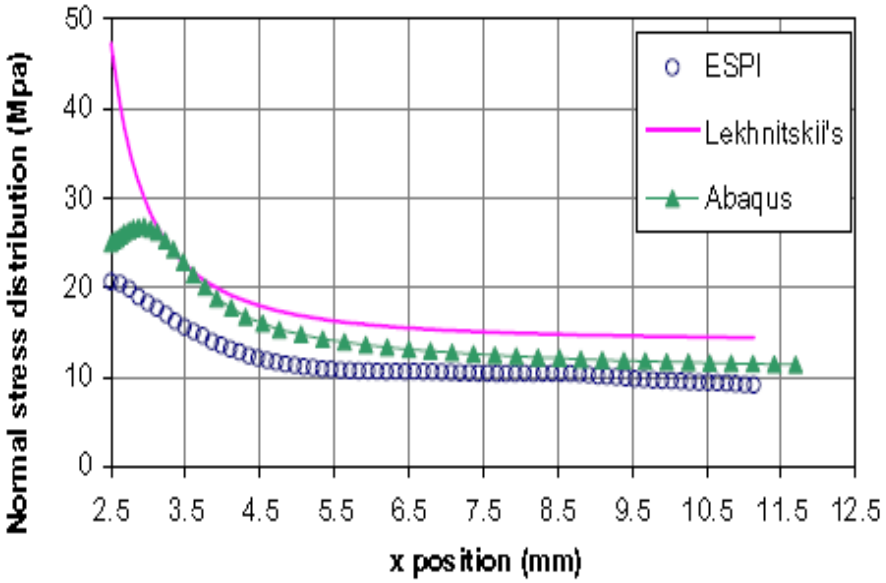

Figure 7-5 Stress distribution of woven fabric composite subject to a tensile load for specimen [±45°] (applied load 810 N) [142]

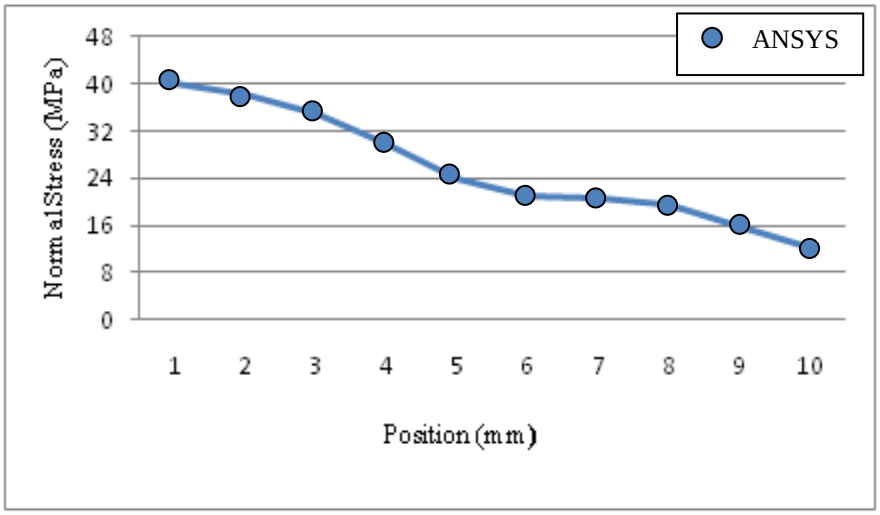

Figure 7-6 Stress distribution (FEA) for carbon epoxy composite plate for 1000N tensile load (Current study)

Chang *et al*. [143] applied tensile loading on a graphite/epoxy composite plate with a hole. The results obtained from the experiment and analytical solutions were found to be almost identical. The specimen was then subjected to increased loading, and the mechanism of initial failure and subsequently progressive failure was observed and modeled in the failure analysis. Increased loading was the primary cause of the damage which could redistribute the stress. Crack initiation and damage propagation was observed when the specimen was subjected to a 9800N load. In the current study, the maximum load applied was 3000N which was well within the linear elastic

limit and did not damage the specimen. The specimen was not tested for failure, making direct comparison of results to the prior study problematic.

7.5 Comparing the Strain Gauge Results with the Literature

Ng *et al.* [125] used a carbon/epoxy plate (E = 143 GPa) with a fibre volume fraction of 52%. The size of the plate was 200 x 25.4 x 1.32 mm^3 and the drilled hole sizes were 3, 6 and 9 mm. It was noted that the strain gauges attached by the side of the hole gave higher values of strain. However, the gauges attached at a distance from the hole gave a relatively uniform strain field. A 2000N load yielded strain values of 1950 and 2025 microstrain around the 6mm diameter hole. In the current study, the strains were measured at 1979 and 1897 microstrain at locations 3 and 4, respectively. The difference of 1.47% and 6.78% showed good agreement in the results between the current and prior study.

7.6 Limitations and Future Work

As the load went beyond 1500N, a significant quantity of slippage was observed at the top edge where the plate was secured in the grips. This problem did not permit the values of stress to be obtained at 2000N and 3000N for lock-in thermography and the strain gauge (cyclic loading) experiment. The values of stress in the lock-in thermography and values of strain in the strain gauge experiment were recorded carefully for 1000N and 1500N loads by constantly observing the force-displacement curve for any inconsistency and slippage. The reason for slippage beyond the 1500N load was that the custom made grips which were not able to secure the top end adequately. This problem could be avoided by using hydraulic grips.

Installation of strain gauges near the edge of the circular hole was a challenge due to the width of the gauge. A stress concentration was observed adjacent to the hole, while the relatively large size of the strain gauges restricted mounting the gauges closer to that area.

Only one specimen was used for testing which can be increased to a number of specimens in the future in order to obtain a comprehensive statistical comparison.

The specimens can be drilled with eccentric holes which may or may not be circular, and the nature of stress concentration should be studied for all cases.

The specimen can be subjected to tensile loading at both ends instead of securing one end in a fixed vice. Using such tension-tension loading, the stress concentration around the hole can be predicated more precisely.

The experiment can be repeated for frequencies other than 5 Hz, and its effect can be investigated.

The influence of short fibres, fibre orientation, the number of fibre layers, and loading conditions can be investigated.

CHAPTER 8. CONCLUSION

In the current study, a specimen plate made of carbon epoxy with a circular hole was experimentally and numerically analyzed to find stresses at various locations. A strong agreement was observed between all the methods.

The experimental and numerical results in the static condition showed that the values of strain were higher in the experimental studies, however strain gauge experiments tended to overestimate the strain results, when compared with FEA. The correlation graphs gave the value of $R^2 = 0.99$ which indicated strong agreement between the two.

In cyclic loading, when the load was applied vertically on the plate, it was observed that the value of stress along the x-axis increased as it approached the hole indicating a stress concentration point at the edge of the hole. The value of stress went up to 69 MPa and 103 MPa for the loads of 1000N and 1500N, respectively. This increment along the x-axis was due to Poisson's effect. The maximum stress was also observed at the top end where the specimen was secured at the grips.

The results from the strain gauge experimental study for cyclic loading at corresponding locations were in good agreement with the results obtained from lock-in thermography within the linear elastic limit. The results were within 12%, while the correlation yielded $R^2 = 0.87$. It was also concluded from all three studies conducted that the maximum stress concentration was around the circular hole, which was the weakest part of the specimen, as expected.

From the current study, it can be stated that nondestructive testing of a carbon epoxy composite plate can be performed successfully by using lock-in thermography. This method can be used to assess stress distribution in biomaterials used in medical applications. It is a non-contact technique producing full stress maps which is an additional advantage over conventional strain gauge experiments.

APPENDICES

APPENDIX 1: Results from Strain Gauge Experiment and Finite Element Study

The values of strain for applied tensile static loads of 1000N, 2000N and 3000N, for strain gauge experiment and FEA model are tabulated below.

Strain Gauge Location	Normal Elastic Strain (με)		% Difference
	Experimental Study	FE Model	
1	1254.00	354.24	71.75
2	962.00	915.89	4.79
3	907.00	952.49	5.02
4	925.00	901.06	2.59
$\% \ Difference = \frac{(\text{Experimental Strain Values - FEA Strain Values}) \times 100}{(\text{Experimental Strain Values})}$			

Table A1- 1 Strain results from the FEA and Strain gauge experimental study for 1000 N

Strain Gauge Location	Normal Elastic Strain (με)		% Difference
	Experimental Study	FE Model	
1	1816.00	679.06	62.61
2	1943.00	1968.00	1.29
3	1979.00	1965.70	0.67
4	1897.00	1867.00	1.58
$\% \ Difference = \frac{(\text{Experimental Strain Values - FEA Strain Values}) \times 100}{(\text{Experimental Strain Values})}$			

Table A1- 2 Strain results from the FEA and Strain gauge experimental study for 2000 N

Strain Gauge Location	Normal Elastic Strain (με)		% Difference
	Experimental Study	FE Model	
1	3885.00	1001.70	74.22
2	3411.00	3397.50	0.40
3	3575.00	3568.70	0.18
4	3516.00	3485.80	0.86

$$\%\ Difference = \frac{(\text{Experimental Strain Values - FEA Strain Values}) \times 100}{(\text{Experimental Strain Values})}$$

Table A1- 3 Strain results from the FEA and Strain gauge experimental study for 3000 N

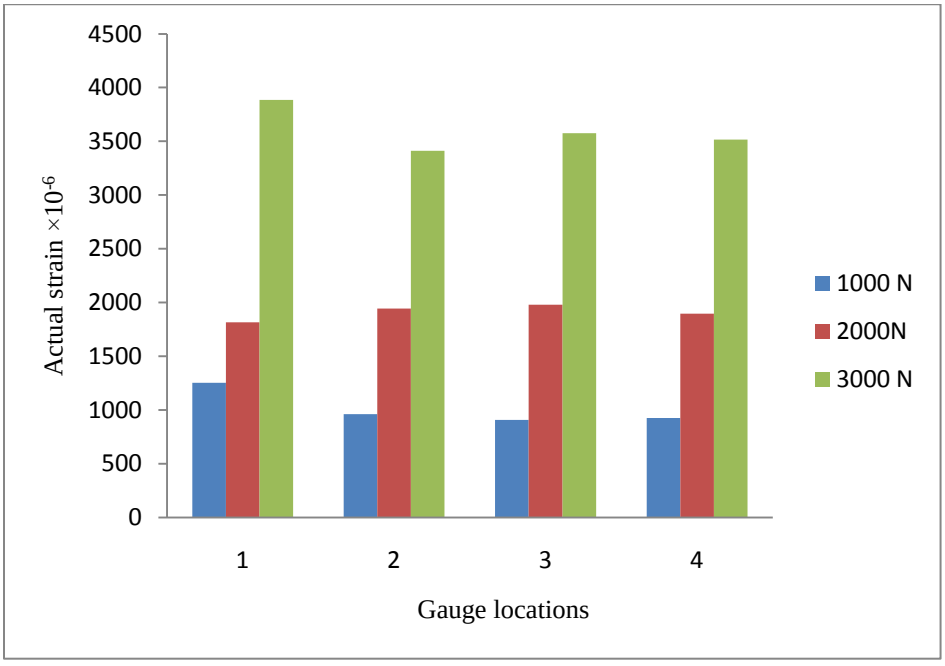

Figure A1- 1 Graphic representation of experimentally measured microstrain values for tensile static loading for strain gauges

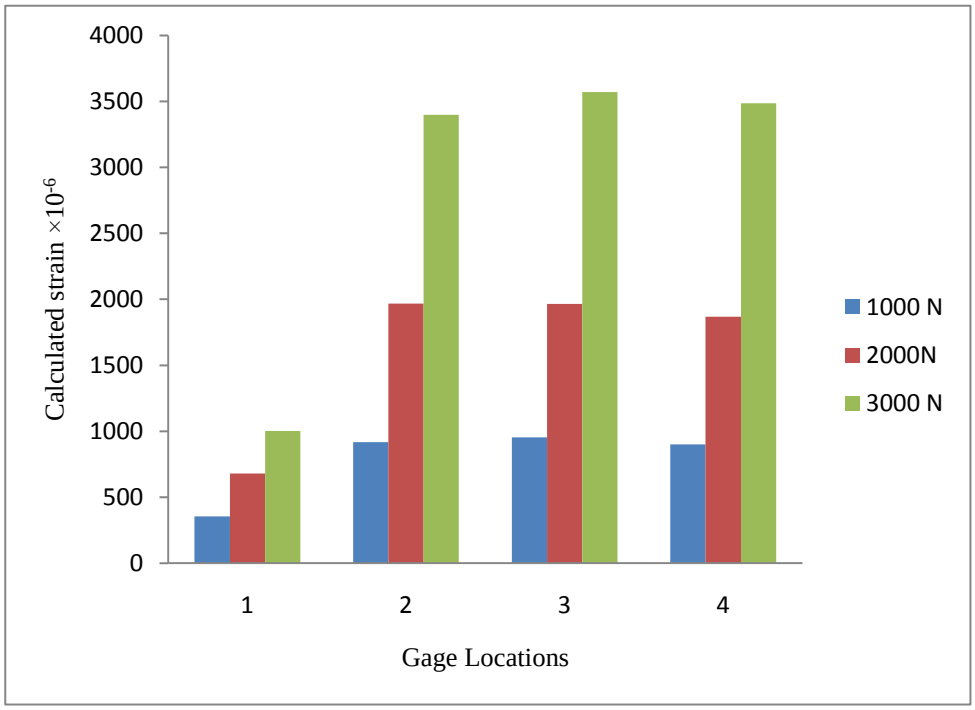

Figure A1- 2 Graphic representation of calculated microstrain values for tensile static condition in FEA

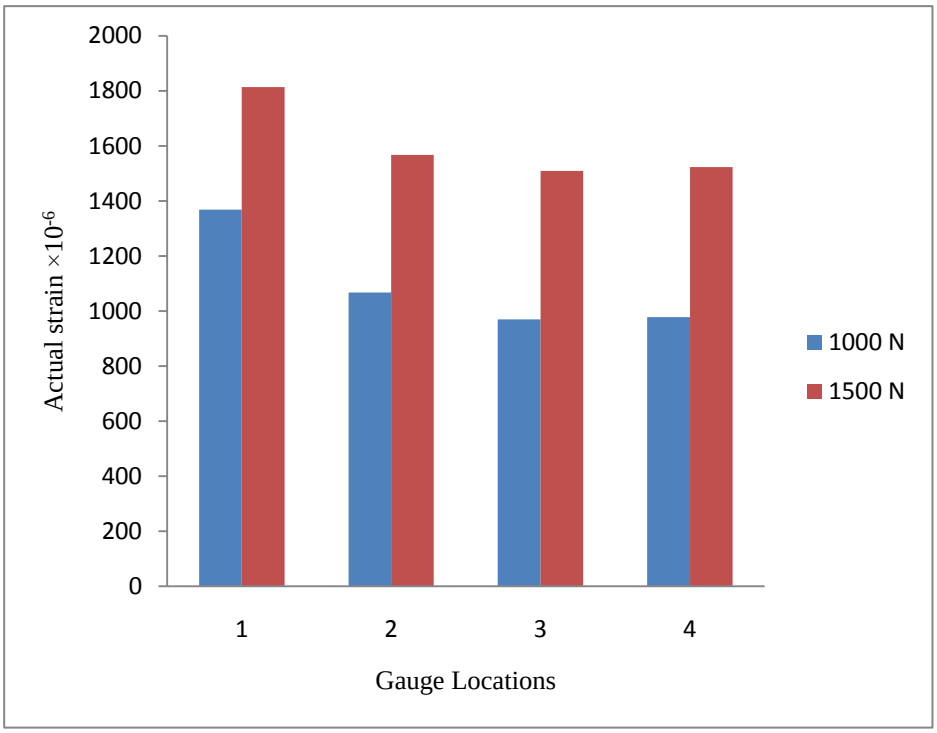

Figure A1- 3 Graph of measured microstrain values for 1000N and 1500N for cyclic loading

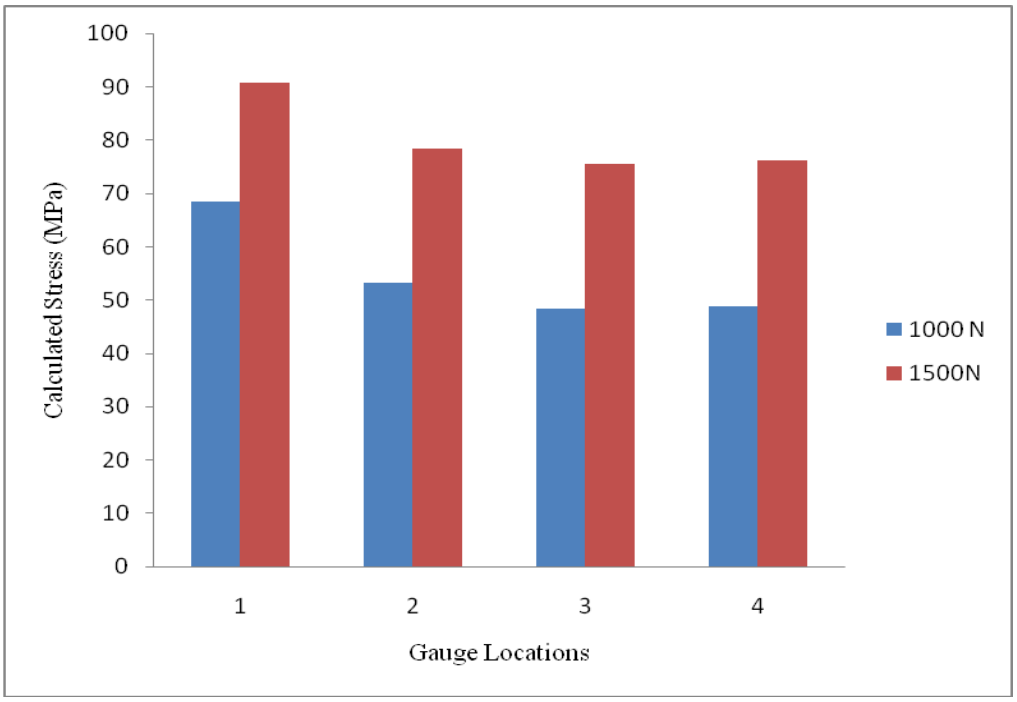

Figure A1- 4 Graph of Stress (MPa) values calculated from strain gauge experiment for 1000 N and 1500 N cyclic loading

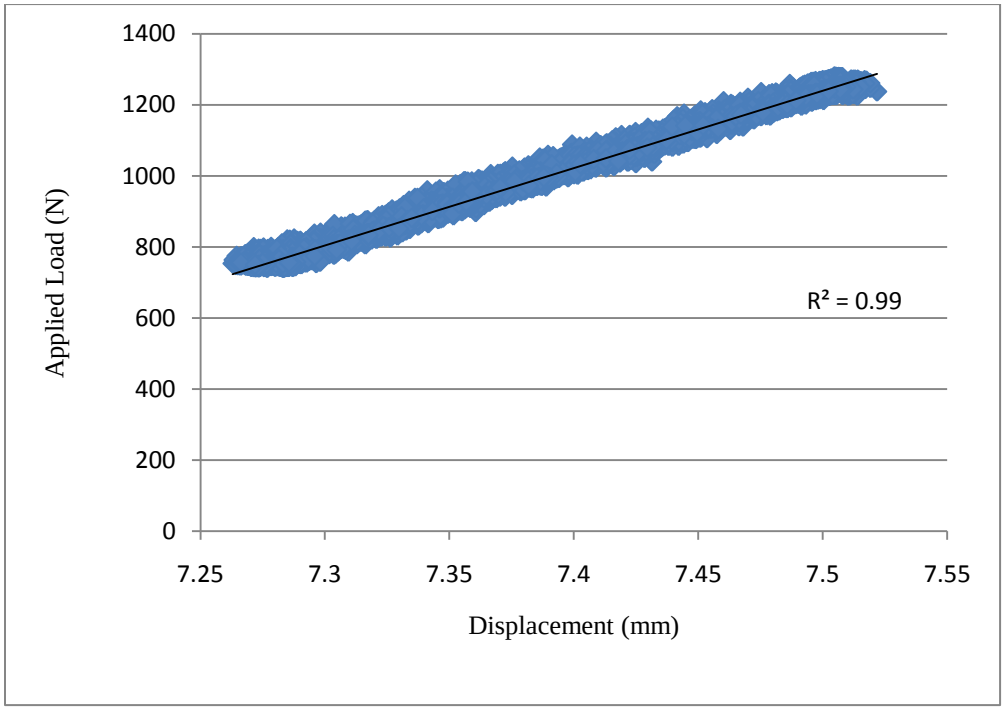

Figure A1- 5 Applied load–displacement curve for 1000N (average) load

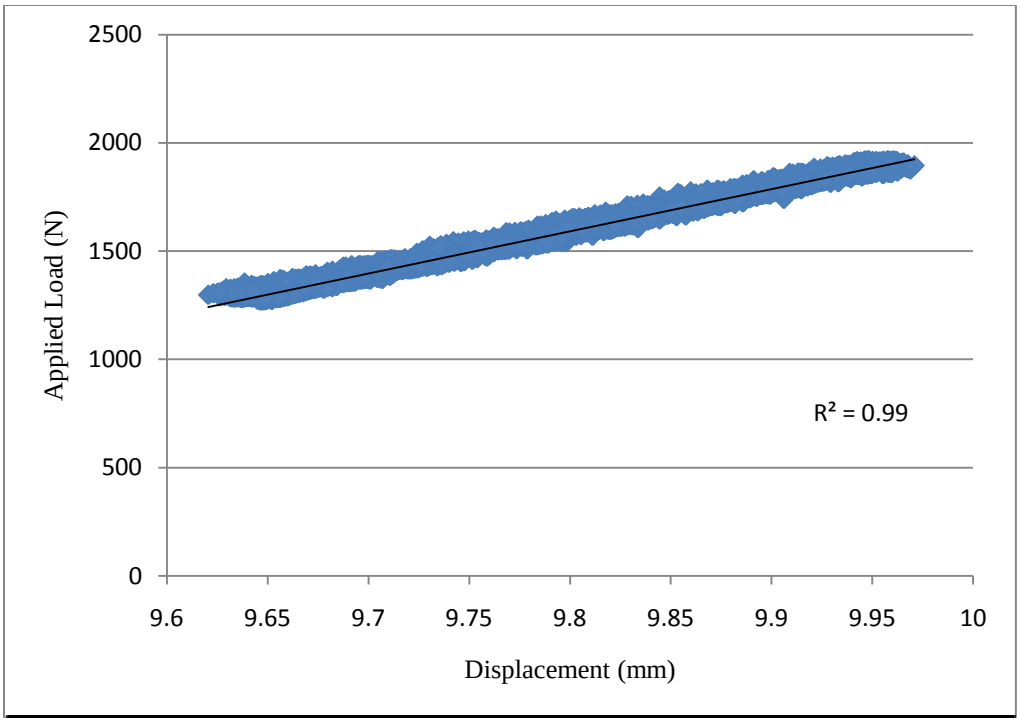

Figure A1- 6 Applied load–displacement curve for 1500 N (average) load

FEA Results (με)	Experimental Strain Gauge Results (με)
354.24	907.00
679.06	925.00
901.06	962.00
915.89	1254.00
952.49	1816.00
1001.70	1897.00
1867.00	1943.00
1965.70	1979.00
1968.00	3411.00
3397.50	3516.00
3485.80	3575.00
3568.70	3885.00

Table A1- 4 Strain values for all FEA and strain gauge experimental results

APPENDIX 2: Finite Element Analysis Stress Maps

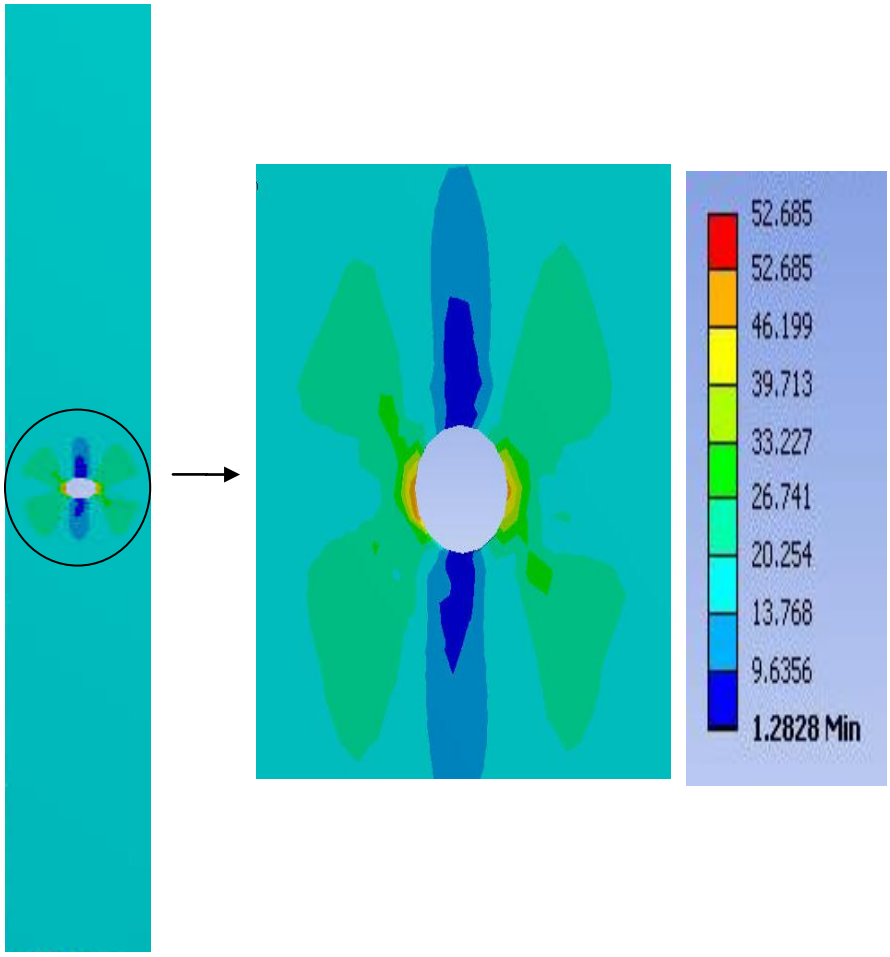

Figure A2- 1 Normal stress (MPa) in the composite plate for 1000 N

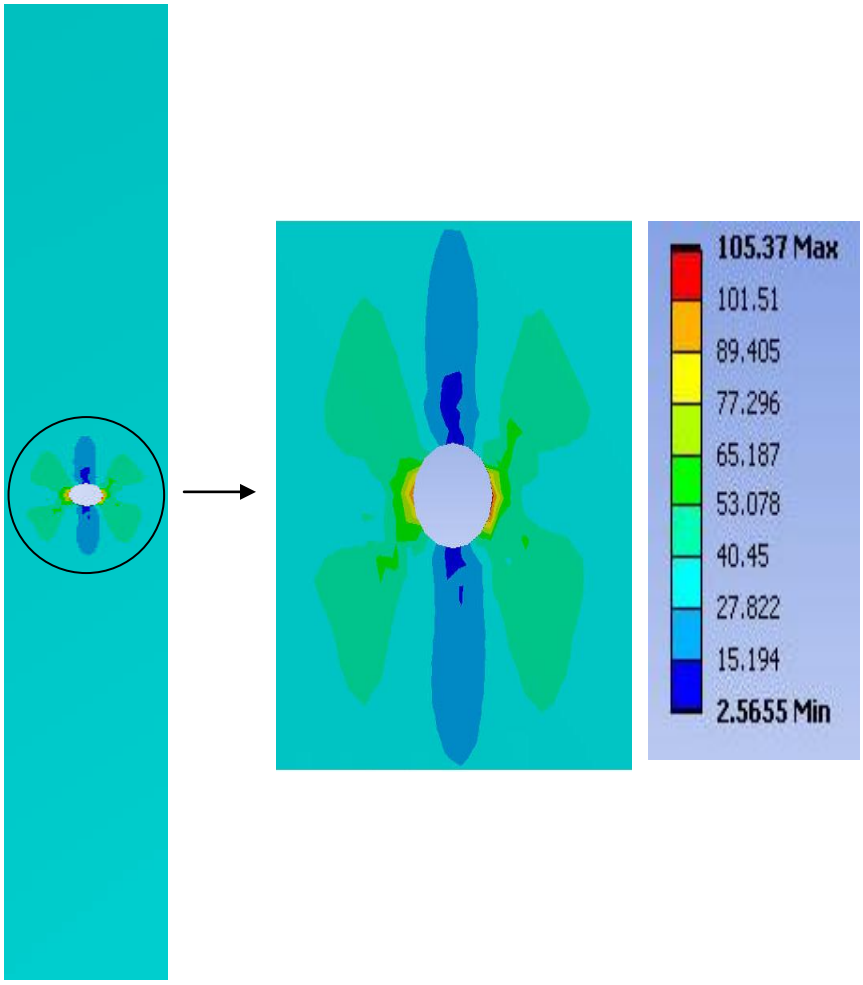

Figure A2- 2 Normal stress (MPa) in the composite plate for 2000 N

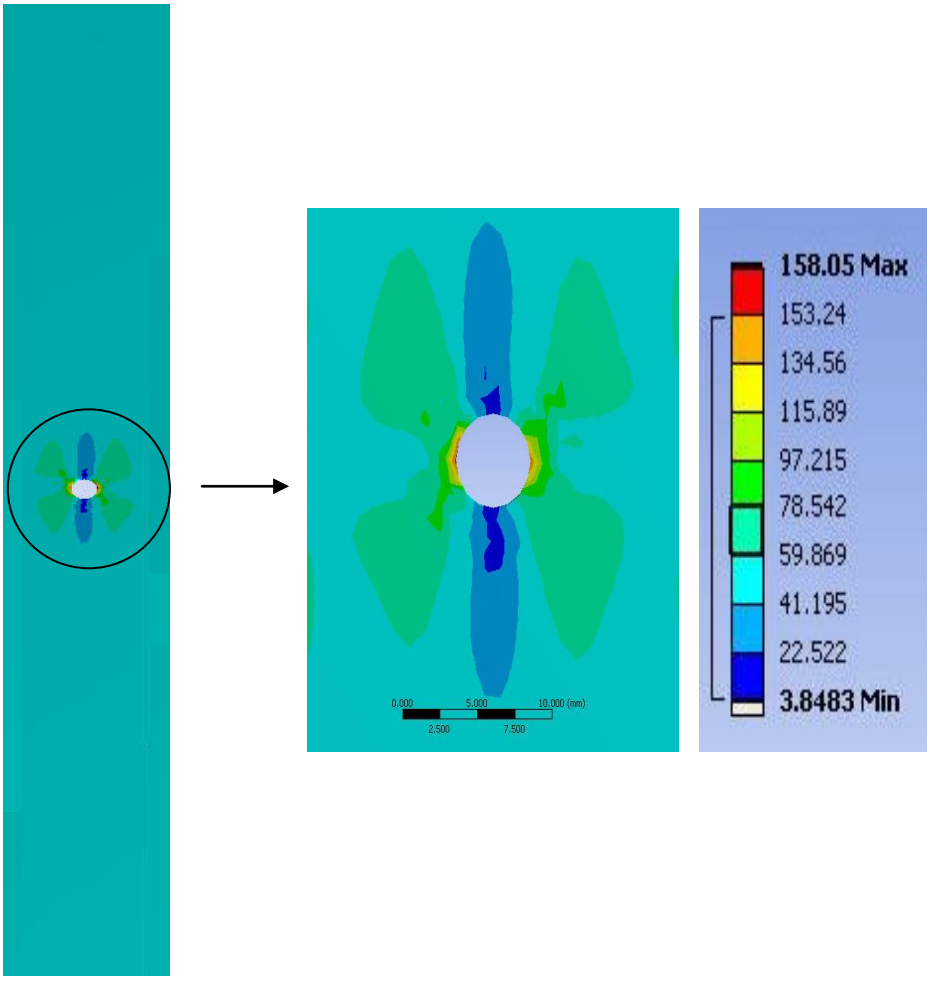

Figure A2- 3 Normal stress (MPa) in the composite plate for 3000 N

APPENDIX 3: Comparison of Stress values from Strain Gauges and IR Tests

Location	Stress (MPa)		% Difference
	Calculated stress values from Strain gauge Experiment	LT Experimental Stress Values	
1	68.40	61.43	10.19
2	53.35	52.81	1.01
3	48.50	52.93	9.13
4	48.90	54.43	11.31
$\%\,Difference = \frac{(\text{Calculated Stress Values - LT Stress Values})}{\text{Calculated Stress Values}} \times 100$			

Table A3- 1 IR and calculated stress values from strain gauge readings for cyclic tensile load of 1000N

Location	Stress (MPa)		% Difference
	Calculated Stress values from Strain gauge Experiment	LT Experimental Stress Values	
1	90.70	86.77	4.33
2	78.38	70.06	10.61
3	75.48	83.48	10.60
4	76.15	84.41	10.85
$\%\,Difference = \frac{(\text{Calculated Stress Values - LT Stress Values})}{\text{Calculated Stress Values}} \times 100$			

Table A3- 2 IR stress values and calculated stress values from strain gauge reading for cyclic tensile load of 1500N

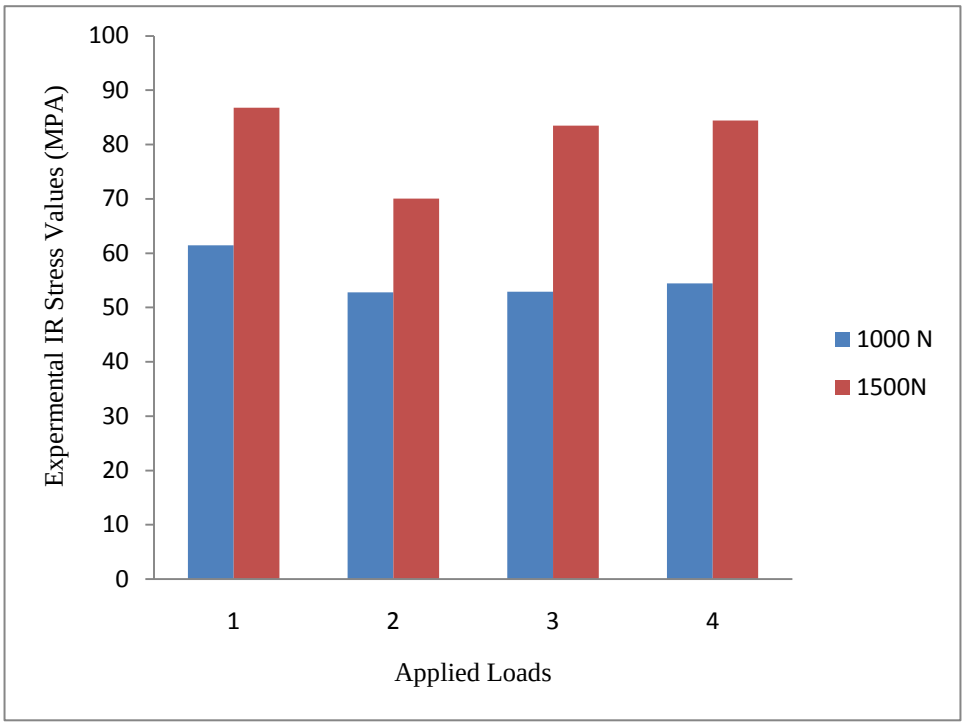

Figure A3- 1 Graph for LT results for 1000N and 1500N cyclic loading

IR values (MPa)	Stress values calculated from experimental Strain gauge results (MPa)
52.81	48.50
52.93	48.90
54.43	53.35
61.43	68.40
70.06	75.48
83.48	76.15
84.41	78.38
86.77	90.70

Table A3- 3 Stress values for all LT and strain gauge experimental results

REFERENCES

[1] Dictionary.com, (2009) Unabridged (v 1.1). Random House, Inc, Accessed December 20, 2009, Available from: <http://dictionary.reference.com/>

[2] Answers.com, (2009) Accessed 20, 2009, Available from: <http://www.answers.com/>

[3] Toubal, L., Karama, M., and Lorrain, B. (2006) "Damage evolution and infrared thermography in woven composite laminates under fatigue loading." International Journal of Fatigue, 28(12), pp. 1867-1872

[4] Mao, H., and Mahadevan, S. (2002) "Fatigue damage modelling of composite materials." Composite Structures, 58(4), pp. 405-410

[5] Bandoh, S., Nakayama, Y., Asagumo, R., and Yoshimura, T. (2003) "Establishment of database of carbon/epoxy material properties and design values on durability and environmental resistance." Advanced Composite Materials, the Official Journal of the Japan Society of Composite Materials, 11(4), pp. 365-374

[6] Toubal, L. (2004), Analytical and experimental approaches of the damage by fatigue of a composite carbon/epoxy. Ph.D. Thesis, University of Toulouse, France

[7] Wróbel, G., Muzia, G., and Pawlak, S. (2008) "Active IR-thermography as a method of fiber content evaluation in carbon/epoxy composites." Materials Science and Engineering, 30(2), pp. 101-104

[8] Harris, B., Gathercole, N., Lee, J. A., Reiter, H., and Adam, T. (1997) "Life-prediction for constant-stress fatigue in carbon-fibre composites." Philosophical Transactions of the Royal Society A: Mathematical, Physical and Engineering Sciences, 355(1727), pp. 1259-1294

[9] Budynas, R. G., and Nisbett, J. K. (2006) Mechanical engineering design (Eighth Edition) McGraw−Hill. pp. 260-336

[10] Pandita, S. D., Nishiyabu, K., and Verpoest, I. (2003) "Strain concentrations in woven fabric composites with holes." Composite Structures, 59(3), pp. 361-368

[11] Ciliberto, A., Cavaccini, G., Salvetti, O., Chimenti, M., Azzarelli, L., Bison, P. G., et al. (2002) "Porosity detection in composite aeronautical structures." Infrared Physics and Technology, 43(3), pp. 139-143

[12] Bates, D., Smith, G., Lu, D., and Hewitt, J. (2000) "Rapid thermal non-destructive testing of aircraft components." Composites Part B: Engineering, 31(3), pp. 175-185

[13] Krishnapillai, M., Jones, R., Marshall, I. H., Bannister, M., and Rajic, N. (2005) "Thermography as a tool for damage assessment." Composite Structures, 67(2), pp. 149-155

[14] Muzia, G., Rdzawski, Z., Rojek, M., Stabik, J., and Wróbel, G. (2007) "Thermographic diagnosis of fatigue degradation of epoxy-glass composites." Journal of Achievements in Materials and Manufacturing Engineering, 24(2), pp. 123-126

[15] Spiessberger, C., Gleiter, A., and Busse, G. (2008) "Aerospace applications of lock-in thermography with optical, ultrasonic, and inductive excitation." International Symposium on NDT in Aerospace, Accessed November 25, 2009, Available from: <http://www.ndt.net/search/docs.php3?MainSource=81>

[16] Tan, S. C., and Kim, R. Y. (1990) "Strain and stress concentrations in composite laminate containing a hole." Experimental Mechanics, 30(4), pp. 345-351

[17] Shepard, S. M. (1997) "Introduction to active thermography for non-destructive evaluation." Anti-Corrosion Methods and Materials, 44(4), pp. 236-239

[18] Meola, C., Carlomagno, G. M., Squillace, A., Prisco, U., and Morace, R. E. (2005) "Analysis of composites with infrared thermography." Macromolecular Symposia, 228(1), pp. 273-286

[19] Wu, D., and Busse, G. (1998) "Lock-in thermography for nondestructive evaluation of materials." Revue Generale De Thermique, 37(8), pp. 693-703

[20] Meola, C., and Carlomagno, G. M. (2006) "Application of infrared thermography to adhesion science." Journal of Adhesion Science and Technology, 20(7), pp. 589-632

[21] Burleigh, D. D. (2002) “A portable, combined thermography/shearography NDT system for inspecting large composite structures.” Proceedings of SPIE, Thermosense XXIV. 4710, pp. 578-587

[22] Avdelidis, N. P. (2007) “A look on thermography: From passive to active NDT & E surveys.” Proceedings of SPIE, Thermosense XXIX, 6541

[23] Charles, J. A., Appl, F. J., and Francis, J. E. (1975) “Using the scanning infrared camera in experimental fatigue studies.” Experimental Mechanics, 15(4), pp. 133-138

[24] Choi, M., Park, J., Kang, K., and Kim, W. (2006) “Application of thermography to analysis of thermal stress in the NDT for compact tensile specimen.” 12th-Asia-Pacific Conference on NDT

[25] Shepard, S. M., Hou, J., Lhota, J. R., and Golden, J. M. (2007) “Automated processing of thermographic derivatives for quality assurance.” Optical Engineering, 46(5), pp. 0510081-6

[26] Avdelidis, N. P., Moropoulou, A., and Almond, D. P. (2004) “Passive and active thermal non-destructive imaging of materials.” Electro-Optical and Infrared Systems: Technology and Applications, Vol. 5612, pp. 126-140

[27] Zauner, G., Mayr, G., and Hendorfer, G. (2006) “Application of wavelet analysis in active thermography for non-destructive testing of CFRP composites.” Wavelet Applications in Industrial Processing IV, 6383(1), pp. 63830E 1-10

[28] Rajaiah, K., and Rao, M. N. R. (1990) “Damage assessment in composites through NDE: Some recent studies in India.” Theoretical and Applied Fracture Mechanics, 13(2), pp. 125-135

[29] Plotnikov, Y. A., and Winfree, W. P. (1999) “Visualization of subsurface defects in composites using a focal plane array infrared camera.” Proceedings of SPIE - the International Society for Optical Engineering, 3700, pp. 26-31

[30] Shirazi, A., and Karbhari, V. M. (2007) "IR thermography as a means of quantifying defects and progression in FRP rehabilitation of concrete." Composite and Polycon, American Composites Manufacturers Association, pp. 1-10

[31] Ray, B. C., Hasan, S. T., and Clegg, D. W. (2007) "Evaluation of defects in FRP composites by NDT techniques." Journal of Reinforced Plastics and Composites, 26(12), pp. 1187-1192

[32] Mallick, P. K. (2008) Fiber-reinforced composites: Materials, manufacturing, and design (Third Edition) CRC Press, Taylor & Francis Group. ISBN: 978-0-8493-4205-9

[33] Busel, P.J. (2006) Report on Fiber-Reinforced Polymer (FRP) Reinforcement for Concrete Structures. pp. 93-100

[34] Gros, X. E. (1997), NDT data fusion. John Wiley & Sons, Inc.

[35] Fike, G. M. (2004) "Using infrared thermography to image the drying of polymer surfaces." M.A.Sc. Thesis. School of Chemical and Biomolecular Engineering, Georgia Institute of Technology, pp. 3-20

[36] Ferraro, C. C. (2003) "Advanced nondestructive monitoring and evaluation of damage in concrete materials." M.A.Sc. Thesis, University of Florida

[37] Larsen, W. E., Cooksy, K. D., and Zuk, J. (2001) "Managing aviation safety through inspection and information technology." IEEE Industry Applications Magazine, 7(3), pp. 40-45

[38] Guo, Y. (2009) The new methods on NDE systems probability of detection (POD) capability assessment and robustness improvement. Ph.D. Thesis. Graduate School of Wayne State University, Detroit, Michigan. pp. 9-32

[39] Emery, T. R. (2007) Identification of damage in composite materials using thermoelastic stress analysis. Ph.D. Thesis. Faculty of engineering, science & mathematics, University of Southampton. pp. 11-26

[40] Hung, Y. Y., Chen, Y. S., Ng, S. P., Liu, L., Huang, Y. H., Luk, B. L., et al. (2009) "Review and comparison of shearography and active thermography for nondestructive evaluation." Materials Science and Engineering R: Reports, 64(5), pp. 73-112

[41] Johnson, S. M. (2006) Infrared thermography and thermoelastic stress analysis of composite materials and structural systems. Master of Science Thesis, School of Civil and Environmental Engineering, Georgia Institute of Technology

[42] Krishnapillai, M., Jones, R., Marshall, I. H., Bannister, M., and Rajic, N. (2006) "NDTE using pulse thermography: Numerical modeling of composite subsurface defects." Composite Structures, 75(1), pp. 241-249

[43] Thompson, J., and Marvin, M. (2005) "Experimental research on the use of thermography to locate heat signatures from caves." National Cave and Karst Management Symposium, pp. 102-115

[44] Rao, M. P. D. (2007) Review of non destructive evaluation techniques for FRP composite structural components. Master of Science Thesis, Department of Civil and Environmental Engineering, College of Engineering and Mineral Resources at West Virginia University, Morgantown, West Virginia. pp. 2-50

[45] Ghosh, K. K., and Karbhari, V. M. (2006) "A critical review of infrared thermography as a method for non-destructive evaluation of FRP rehabilitated structures." International Journal of Materials and Product Technology, 25(4), pp. 241-266

[46] Huang, S., Li, L., Yang, H., and Shi, K. (2003) "NDE of composites delamination by infrared thermography." NDE and Health Monitoring of Aerospace Materials and Composites II, 5046, pp. 219-223

[47] Shepard, S. M. (2007) "Thermography of composites." Accessed November 25, 2009, from: http://www.asnt.org/publications/materialseval/basics/jul07basics/jul07basics.htm in http://www.asnt.org/publications/materialseval/basicsarchive.htm

[48] Meola, C., Carlomagno, G. M., and Giorleo, L. (2004) "The use of infrared thermography for materials characterization." Journal of Materials Processing Technology, 155(1), pp. 1132-1137

[49] Cantwell, W. J., and Morton, J. (1992) "Significance of damage and defects and their detection in composite materials, A review." Journal of Strain Analysis for Engineering Design, 27(1), pp. 29-42

[50] Kawazoe, Y. (2009) High temperature measurements of materials. Springer

[51] Siegel, R., and Howell, J. R. (1968) "Thermal radiation heat transfer." Scientific and technical Information division, National aeronautics and space administration, Washington D.C. Vol. 1

[52] Lantada, A. D., Morgado, P. L., Lorenzo-Yustos, H., Muñoz-García, J., Sanz, J. L. M., Otero, J. E., et al. (2009) "Infrared thermography as a support tool for developing shape-memory polymer biodevices." in Biodevices, Second International Conference on Biomedical Electronics and devices. pp. 145-150

[53] Mix, P. E. (2005) Introduction to non destruction testing, a training guide. (Second Edition) A John Wiley & Sons, Inc

[54] Brown, J. R. (2005) Infrared thermography inspection of fiber reinforced polymer composites bonded to concrete. Ph.D. Thesis, University of Florida. pp. 18-35

[55] Maldague, X. (2000) "Applications of infrared thermography in nondestructive evaluation." Electrical and Computing Engineering Department, University of Laval, Quebec City, pp. 1-23

[56] Ammirato, F., and Zayicek, P. (1999) Infrared thermography field application guide. EPRI, Palo Alto, CA: 1999. Report TR-107142

[57] Scheffer, C. (2004) Practical machinery vibration analysis and predictive maintenance. Oxford, Elsevier

[58] Winsor, T., and Winsor, D. (1985) “The noninvasive laboratory - history and future of thermography”. Angiology, 36(6), pp. 341-353

[59] Infrared thermography education & support. (2009). Accessed December 27, 2009, Available from: <http://www.infraredinstitute.com/>

[60] Chaudhuri, P., Santra, P., Yoele, S., Prakash, A., Reddy, D. C., Lachhvani, L. T., et al. (2006) “Non-destructive evaluation of brazed joints between cooling tube and heat sink by IR thermography and its verification using FE analysis.” NDT and E International, 39(2), pp. 88-95

[61] Gauglitz, G., and Vo-Dinh, T. (2003) Handbook of spectroscopy. Wiley-VCH Verlag GmbH & Co. pp. 268-294

[62] UK thermography association. (2009) Accessed December 27, 2009, Available from: <http://www.ukta.org/>

[63] Cool Cosmos from Infrared Processing and Analysis Center, Science and data center for infrared astronomy, “Discovery of infrared.” (2009) Accessed October 29, 2009, Available from: <http://coolcosmos.ipac.caltech.edu/cosmic_classroom/classroom_activities/herschel_bio.html>

[64] Fickes, L. (2009) “History of thermography.” Accessed December 30, 2009, Available from: <http://www.holisticcarehawaii.com/history.htm>

[65] Meola, C., and Carlomagno, G. M. (2004) “Recent advances in the use of infrared thermography.” Measurement Science and Technology, 15(9), pp. 27-58

[66] Meola, C., Giorleo, G., Nele, L., Squillace, A., and Carlomagno, G. M. (2002) “Infrared thermography in the quality assurance of manufacturing systems.” Nondestructive Testing and Evaluation, 18(2), pp. 83-90

[67] Omar, M. A., Zhou, Y., and Liu, J. (2007) “Automated applications of the infrared imagers in the automotive assembly lines: Products and process control.” 6541, pp. 65410E1-8

[68] Bates, D., Smith, G., Lu, D., and Hewitt, J. (2000) "Rapid thermal non-destructive testing of aircraft components." Composites Part B: Engineering, 31(3), pp. 175-185

[69] Shepard, S. M. (2003) "Advances in thermographic NDT." Infrared Technology and Applications, 5074, pp. 882-887

[70] Fan, C. L., Sheng, L. H., Li, M. L., Yang, L., and Sun, F. R. (2006) "Study on thermographic inspection of pipelines used in vessel and its insulation layer." Journal of Electron Devices, 29(4), pp. 1367-1371

[71] Avdelidis, N. P., Almond, D. P., Dobbinson, A., Hawtin, B., Ibarra-Castanedo, C., and Maldague, X. (2004) "Thermal transient thermographic NDT & E of composites." Proc. of SPIE, 5405, pp. 403-413

[72] Lisboa, F. (2003) "Thermal imaging for predictive maintenance." Diesel and Gas Turbine Worldwide, 35(6), pp. 48-49

[73] Delo, M., and Delo, S. (2007) "Infrared thermographic diagnostic aid to aircraft maintenance." Proc. of SPIE, 6541

[74] Zauner, G., Mayr, G., and Hendorfer, G. (2009) "Comparative defect evaluation of aircraft components by active thermography." SPIE, Image Processing: Machine Vision Applications II, 7251, pp. 1-9

[75] Castanedo, C. I., (2005) Quantitative subsurface defect evaluation by pulsed phase thermography: Depth retrieval with the phase. Ph.D. Thesis, University Laval, Quebec, pp. 6-26

[76] Galmiche, F., and Maldague, X., (1999) "Active infrared thermography for land mine detection." Conference on Diagnostic Imaging Technologies and Industrial Applications Munich, Germany, SPIE, 3827, pp. 146-154

[77] Ibarra-Castanedo, C., Piau, J., Guilbert, S., Avdelidis, N., Genest, M., Bendada, A., et al. (2009) "Comparative study of active thermography techniques for the nondestructive evaluation of honeycomb structures." Research in Nondestructive Evaluation, 20(1), pp. 1-31

[78] Chen, Y. S., Hung, Y. Y., and Liu, L., (2008) "Electro-thermography technique for nondestructive testing (NDT) applications." Proc. of SPIE, ICEM: International Conference on Experimental Mechanics, 7375, pp. 737540-6

[79] Meola, C., Carlomagno, G. M., and Giorleo, L. (2004) "Geometrical limitations to detection of defects in composites by means of infrared thermography." Journal of Nondestructive Evaluation, 23(4), pp. 125-132

[80] Bai, W., and Wong, B. S. (2001) "Evaluation of defects in composite plates under convective environments using lock-in thermography." Measurement Science and Technology, 12(2), pp. 142-150

[81] Tarin, M., and Kasper, A. (2008) "Fuselage inspection of boeing-737 using lock-in thermography." Proc. of SPIE, Thermosense XXX, 6939, pp. 1-10

[82] Huth, S., Breitenstein, O., Huber, A., Dantz, D., Lambert, U., and Altmann, F. (2002) "Lock- in IR-thermography - A novel tool for material and device characterization" Diffusion and Defect Data, Part.B: Solid State Phenomena, 82, pp. 741-776

[83] Wang, X., Crupi, V., Zhao, Y., and Guo, X. (2009) "Lock-in thermographic methodology for fatigue assessment and nonlinear stress measurement." Proc. of SPIE, ICEM 2008: International Conference on Experimental Mechanics. 7375, pp. 1-6

[84] Zhao, Y., Guo, X., Ren, M., Wang, X., and He, Y. (2009) "Lock-in thermography method for the NDT of composite materials." International Conference on Experimental Mechanics, 7375, pp. 1-6

[85] Zweschper, T., Dillenz, A., Riegert, G., and Busse, G. (2002) "Lock-in thermography mehods for the NDT of CFRP aircraft components." NDT, 8th ECNDT, Barcelona, Available from: <http://www.ndt.net/article/ecndt02/249/249.htm>, 8(2)

[86] Wang, Z., Liu, J., and Dai, J. (2007) "Lock-in thermography for evaluation of destruction area and determination of depth." Optical Test and Measurement Technology and Equipment, 6723, pp. 67231F1-5

[87] Menner, P., Gerhard, H., and Busse, G. (2008) “Lock-in speckle-interferometry for non-destructive testing.” 7063, pp. 70630C-1

[88] Gleiter, A., Spießberger, C., and Busse, G. (2009) “Lock-in thermography with optical or ultrasound excitation.” 10th International Conference of the Slovenian Society for Non-Destructive Testing, Application of Contemporary Non-Destructive Testing in Engineering, pp. 447-454

[89] Meola, C., Carlomagno, G. M., Squillace, A., and Vitiello, A. (2006) “Non-destructive evaluation of aerospace materials with lock-in thermography.” Engineering Failure Analysis, 13(3), pp. 380-388

[90] Bai, W., and Wong, B. S. (2000) “Non-destructive evaluation of aircraft structure using lock-in thermography.” 3994, pp. 37-46

[91] Liu, J., Dai, J., and Wang, Y. (2009) “Research on lock in thermography for aerospace materials of nondestructive test based on image sequence processing.” Proceedings Vol. 7375, ICEM 2008: International Conference on Experimental Mechanics 2008, Xiaoyuan He, Huimin Xie, and YiLan Kang, Editors

[92] Tarin, M., and Kasper, A. (2008) “Fuselage inspection of boeing-737 using lock-in thermography.” 6939, pp. 1-10

[93] Thomas, R. A., Jones, N., and Donne, K. E. (2000) “Infrared thermography and diagnostic monitoring.” Journal of Imaging Science, 48(1), pp. 23-32

[94] Maldague, X. P. V. (2002) “Introduction to NDT by active infrared thermography.” Materials Evaluation, 60(9), pp. 1060-1073

[95] Carino, N. J., and Malhotra, V. M. (2004) “Nondestructive testing of concrete." in Handbook on Infrared Thermographic Techniques (Second Edition). ASTM International, West Conshohocken, PA: CRC Press, pp. 384-386

[96] Hawkins, G. F., Johnson, E. C., and Nokes, J. P. (1999) "Detecting manufacturing flaws in composite retrofits." Proceedings of SPIE - The International Society for Optical Engineering, 3587, pp. 97-104

[97] Ng, E. Y. (2009) "A review of thermography as promising non-invasive detection modality for breast tumor." International Journal of Thermal Sciences, 48(5), pp. 849-859

[98] Castanedo, C., Genest, M., Piau, J. M., Guibert, S., Bendada, A., and Maldague, X. P. V. (2007) "Quantitative evaluation of emerging infrared thermography technologies for aerospace applications." Ultrasonic and advanced methods for nondestructive testing and material characterization. pp. 325-348

[99] Cramer, K. E., and Winfree, W. P. (1998) "Thermographic detection and quantitative characterization of corrosion by application of thermal line source." 3361, pp. 291-300

[100] Yang, B. (2003) Thermography detection on the fatigue damage. Ph.D. Thesis, The University of Tennessee, Knoxville

[101] Sham, F. C., Huang, Y. H., Liu, L., Chen, Y. S., Hung, Y. Y., and Lo, T. Y. (2010) "Computerized tomography technique for reconstruction of obstructed temperature field in infrared thermography." Infrared Physics and Technology, 53(1), pp. 1-9

[102] Gergenova, Z. V., Nesteruk, D. A., and Shiryaev, V. V. (2005) "Infrared thermographic nondestructive testing system." 11th International Scientific and Practical Conference of Students, Postgraduates and Young Scientists; Modern Technique and Technologies 2005 - Proceedings, pp. 182-183

[103] Howell, P. A., Winfree, W. P., and Cramer, K. E. (2008) "On-orbit passive thermography." Nondestructive Testing and Evaluation, 23(3), pp. 195-210

[104] Kunc, P., Prikryl, M., and Maloun, J. (2007) "Infrared thermography as a tool to study the milking process: A review." Agriculture Tropics and Subtropics, 40(1), pp. 29-32

[105] Minkina, W., and Dudzik, S. (2009) Infrared thermography, errors and uncertainties, Wiley and sons ltd

[106] Krutop, B.N.E. (2007) Effect of impact damage and subsequent fatigue damage development in carbon fiber polymer composites for aircraft. M.Sc. Thesis, Cranfield University, pp. 1-28

[107] Guo, H., Huang, Y., Liu, L., and Shi, X. (2010) "Effect of epoxy coatings on carbon fibers during manufacture of carbon fiber reinforced resin matrix composites." Materials and Design, 31(3), pp. 1186-1190

[108] www.speedace.info, Composite materials, (2010) Accessed June 26, 2010, Available from: <http://www.solarnavigator.net/composites/composite_materials.htm>

[109] Mukundan, S. (2003) Structural design and analysis of a lightweight composite sandwich space radiator panel. Master of Science, Mechanical Engineering, Texas A&M University

[110] Miracle, D.B., Donaldson, S.L., Editors (2001) ASM Handbook: Composites (Vol. 21), ASM 2001

[111] Curtis, P. T. (1989) "The fatigue of organic matrix composite materials", in Advanced composites, Elsevier. pp. 331-367

[112] Chowdhury, K. A. (2007) Damage initiation, progression and failure of polymer matrix compositions due to manufacturing induced defects. Ph.D. Thesis, Aerospace Engineering, Texas A&M University, pp. 2-28

[113] Paepegem, W. V. (2002) Development and finite element implementation of a damage model for fatigue of fibre-reinforced polymers. Ph.D. Thesis, University of Gent, Ghent, Belgium, pp. 1-23

[114] Mazumdar, S. K. (2002) Composites manufacturing materials, product, and process engineering. CRC Press

[115] Vasiliev, V. V., and Morozov, E. V. (2001) Mechanics and analysis of composite materials (First Edition.) Elsevier. pp. 1-27

[116] Matthews, F. L., Davies, G. A., Hitchings, D., and Soutis, C. (2000) "Finite element modelling of composite materials and structures" Woodhead Publishing Limited: Cambridge England

[117] Mallick, P. K. (1997). Composites engineering handbook. Materials engineering, Marcel Dekker, Inc. New York

[118] Menard, K. P. (2008) Dynamic mechanical analysis, A Practical introduction. (Second Edition). 6000 Broken Sound Parkway NW, Suite 300 Boca Raton, FL 33487-2742: Taylor & Francis Group. pp. 123-142

[119] Zhou, Y., Mahfuz, H., Rangari , V., and Jeelani, S. (2008) "An experimental and analytical study of unidirectional carbon fiber reinforced epoxy modified by silicon carbide nanoparticle." in "Composite materials research progress". Center for Advanced Materials at Tuskegee University. pp. 129-164

[120] Baker, A., Dutton, S., and Kelly, D. (2007) Composite materials for aircraft structures. (Second Edition) American Institute of Aeronautics and Astronautics Inc. 1801 Alexander Bell Drive, Reston, VA. pp. 55-80

[121] Frédéric, J., and Sylvain, F. (2008) "Multi-scale analysis of fiber-reinforced composite parts submitted to environmental and mechanical loads" in Composite materials research progress. Nova Science Publishers, Inc. New York. pp. 1-50

[122] Kreculj, D. D. (2008) "Stress analysis in an unidirectional Carbon/Epoxy composite material." FME Transactions, 36, pp. 127-132

[123] Backlund, J., and Aronsson, C. (1986) "Tensile Fracture of Laminates with holes." Journal of Composite Materials, 20(3), pp. 259-286

[124] Bailie, J. A., Duggan, M. F., Fisher, L. M., and Yee, R. C. (1982) “Effects of holes on graphite cloth epoxy laminates tension strength.” Journal of Aircraft, 19(7), pp. 559-566

[125] Ng, S., Lau, K. J., and Tse, P. C. (2000) “3D finite element analysis of tensile notched strength of 2/2 twill weave fabric composites with drilled circular hole.” Composites Part B: Engineering, 31(2), pp. 113-132

[126] Szivek, J. A., and Gharpuray, V. M. (2000) "Strain gauge measurements from bone surfaces" in, Mechanical testing of bone and the bone-implant interface, CRC Press, Boca Raton, FL. pp. 305-320

[127] Coope, M. (2010) "How they work: The strain gauge." Sensorland.com, the online information centre for sensing and measurement. Accessed June 5, 2010, Available from: <http://www.sensorland.com/HowPage002.html>

[128] Vishay micro-measurements. (2010) "General purpose strain gages." Accessed June 2, 2010, Available from: <http://www.vishay.com/docs/11349/11349.pdf>

[129] Surface preparation for strain gage bonding. (2009) Accessed May 5, 2010, Available from: <http://www.vishay.com/docs/11129/11129_b1.pdf>

[130] Hodgkinson, J. M. (Ed.). (2000) Mechanical testing of advanced fibre composites. Woodhead Publishing Limited: Cambridge, England, pp. 248-266

[131] Vishay Micro-Measurements. “The three-wire quarter-bridge circuit.” (2007) Accessed June 5, 2010, Available from: <http://www.vishay.com/docs/11092/tt612.pdf>

[132] Vishay Micro-Measurements. “Three Leadwire Attachment.” (2005) Accessed June 5, 2010, Available from: <http://www.vishay.com/docs/11185/vmm-21.pdf>

[133] Instruments, N. “Choosing the right strain-gauge for your application.” (2010). Accessed June 5, 2010, Available from: <http://zone.ni.com/devzone/cda/tut/p/id/3092#toc2>

[134] “8874 Axial-torsion fatigue testing systems.” (2010) Accessed June 5, 2010, Available from: <http://www.instron.us/wa/product/8874-AxialTorsion-Fatigue-Testing-System.aspx>

[135] Giorleo, G., and Meola, C. (1998) “Location and geometry of defects in composite laminates from infrared images.” Journal of Materials Engineering and Performance, 7(3), pp. 367-374

[136] Cedip infrared systems, in Altair-L1, Instruction manual. (2009)

[137] Silver user Manual, Cedip infrared system (2009). 1-23

[138] Aktas, A., and Dirikolu, M. H. (2003) “The effect of stacking sequence of carbon epoxy composite laminates on pinned-joint strength.” Composite Structures, 62(1), pp. 107-111

[139] De Moura, M. F. S. F., Gonçalves, J. P. M., Marques, A. T., and De Castro, P. M. S. T. (2000) “Prediction of compressive strength of carbon-epoxy laminates containing delamination by using a mixed-mode damage model.” Composite Structures, 50(2), pp. 151-157

[140] Aslan, Z., Karakuzu, R., and Okutan, B. (2003) “The response of laminated composite plates under low-velocity impact loading.” Composite Structures, 59(1), pp. 119-127

[141] “Material properties.” Accessed December 21, 2009, Available from: <http://www.efunda.com/materials/polymers/properties/polymer_datasheet.cfm?MajorID=epoxy&MinorID=5>

[142] Toubal, L., Karama, M., and Lorrain, B. (2005) “Stress concentration in a circular hole in composite plate.” Composite Structures, 68(1), pp. 31-36

[143] Chang, F., and Chang, K. (1987) “Progressive damage model for laminated composites containing stress concentrations.” Journal of Composite Materials, 21(9), pp. 834-855